

# A late Paleoproterozoic (1.74 Ga) deep-sea, low-temperature, iron-oxidizing microbial hydrothermal vent community from Arizona, USA

Crispin T. S. Little<sup>1</sup>  | Karen C. Johannessen<sup>2</sup>  | Stefan Bengtson<sup>3</sup>  |  
 Clara S. Chan<sup>4</sup>  | Magnus Ivarsson<sup>3,5</sup> | John F. Slack<sup>6</sup>  | Curt Broman<sup>7</sup> |  
 Ingunn H. Thorseth<sup>2</sup>  | Tor Grenne<sup>8</sup>  | Olivier J. Rouxel<sup>9</sup>  | Andrey Bekker<sup>10,11</sup> 

<sup>1</sup>School of Earth and Environment,  
University of Leeds, Leeds, UK

<sup>2</sup>Department of Earth Science, University of  
Bergen, Bergen, Norway

<sup>3</sup>Department of Palaeobiology, Swedish  
Museum of Natural History, Stockholm,  
Sweden

<sup>4</sup>Department of Earth Sciences, University  
of Delaware, Newark, USA

<sup>5</sup>Department of Biology, University of  
Southern Denmark, Odense M, Denmark

<sup>6</sup>U.S. Geological Survey (Emeritus), National  
Center, Reston, USA

<sup>7</sup>Department of Geological Sciences,  
Stockholm University, Stockholm, Sweden

<sup>8</sup>Geological Survey of Norway, Trondheim,  
Norway

<sup>9</sup>Marine Geosciences Research Unit,  
IFREMER, Plouzané, France

<sup>10</sup>Department of Earth and Planetary  
Sciences, University of California, Riverside,  
USA

<sup>11</sup>Department of Geology, University of  
Johannesburg, Johannesburg, South Africa

## Correspondence

Crispin T. S. Little, School of Earth and  
Environment, University of Leeds, Leeds LS2  
9JT, UK.

Email: earctsl@leeds.ac.uk

## Funding information

Research Council of Norway Grant (197411/  
V30). Swedish Research Council Contracts  
No. 2012-4364 and 2017-04129. Villum  
Investigator Grant (No. 16518).

## Abstract

Modern marine hydrothermal vents occur in a wide variety of tectonic settings and are characterized by seafloor emission of fluids rich in dissolved chemicals and rapid mineral precipitation. Some hydrothermal systems vent only low-temperature Fe-rich fluids, which precipitate deposits dominated by iron oxyhydroxides, in places together with Mn-oxyhydroxides and amorphous silica. While a proportion of this mineralization is abiogenic, most is the result of the metabolic activities of benthic, Fe-oxidizing bacteria (FeOB), principally belonging to the Zetaproteobacteria. These micro-organisms secrete micrometer-scale stalks, sheaths, and tubes with a variety of morphologies, composed largely of ferrihydrite that act as sacrificial structures, preventing encrustation of the cells that produce them. Cultivated marine FeOB generally require neutral pH and microaerobic conditions to grow. Here, we describe the morphology and mineralogy of filamentous microstructures from a late Paleoproterozoic (1.74 Ga) jasper (Fe-oxide-silica) deposit from the Jerome area of the Verde mining district in central Arizona, USA, that resemble the branching tubes formed by some modern marine FeOB. On the basis of this comparison, we interpret the Jerome area filaments as having formed by FeOB on the deep seafloor, at the interface of weakly oxygenated seawater and low-temperature Fe-rich hydrothermal fluids. We compare the Jerome area filaments with other purported examples of Precambrian FeOB and discuss the implications of their presence for existing redox models of Paleoproterozoic oceans during the “Boring Billion.”

## KEYWORDS

Arizona, Fe-oxidizing bacteria, hydrothermal vents, jasper, late Paleoproterozoic, Verde mining district

This is an open access article under the terms of the Creative Commons Attribution License, which permits use, distribution and reproduction in any medium, provided the original work is properly cited.

© 2021 The Authors. *Geobiology* published by John Wiley & Sons Ltd.

## 1 | INTRODUCTION

In the decades since their first discovery in 1977, marine hydrothermal vents have been reported from all of the world's oceans in a wide variety of tectonic settings where a heat source is present, including at more than 400 sites on mid-ocean ridges, fore- and back-arc spreading centers, arc volcanoes, and intra-plate volcanoes and seamounts (e.g., Beaulieu et al., 2013; Corliss et al., 1979; Fouquet et al., 2010; Karl et al., 1988; Pedersen et al., 2010; Petersen et al., 2019). Many of these hydrothermal systems are characterized by seafloor emission of high-temperature (up to 400°C) fluids rich in dissolved chemicals, which rapidly precipitate chimney and mound structures formed largely of metal sulfides (e.g., pyrite, chalcopyrite, sphalerite), sulfates (e.g., anhydrite, barite), and silica (e.g., Hannington, 2014; Hannington et al., 1995; Tivey, 2007). However, most hydrothermal fluid exits the seafloor at lower temperatures (in the 10 s of °C) and typically is much lower in dissolved chemicals, because of mixing with ambient seawater in the subsurface. The resulting hydrothermal seafloor precipitates commonly have a different mineralogy (e.g., Fe-oxides and iron oxyhydroxides) to those that form from high-temperature fluids. Some marine hydrothermal systems only vent low-temperature fluids, and these are characterized by the precipitation of Fe-oxide-rich deposits that display a wide variety of morphologies from layered sediments to small-scale chimney structures (e.g., Hein et al., 2008; Sun et al., 2013, 2015 and references therein). Such deposits occur at the interface where

anoxic, Fe-rich, S-poor, low-temperature (10 s of °C) hydrothermal fluids mix with oxygenated seawater at ambient temperatures (e.g., Edwards et al., 2011; Emerson et al., 2007; Forget et al., 2010; Glazer & Rouxel, 2009; Langley et al., 2009; Sun et al., 2013). The mineralogy of these hydrothermal Fe-rich deposits is dominated by iron oxyhydroxides (e.g., ferrihydrite and goethite), commonly accompanied by Mn-oxyhydroxides and locally with significant amounts of amorphous silica (e.g., Dekov et al., 2015; Jones et al., 2008; Li et al., 2012; Peng et al., 2015; Rouxel et al. 2018; Toner et al., 2012); hematite (Fe<sub>2</sub>O<sub>3</sub>) has been reported from only one, higher-temperature site (estimated to be ≥115°C; Hein et al., 2008).

While some of the iron oxyhydroxide precipitation in these systems is abiogenic (occurring as micrometer-scale Fe-oxide particles), it is now well established that a proportion, and generally the majority, of the volume of iron oxyhydroxide precipitate is formed by benthic, Fe-oxidizing bacteria (FeOB), principally belonging to the Zetaproteobacteria (Chan, Emerson & Luther, 2016; Chan et al., 2011; Chan, McAllister, et al., 2016; Davis & Moyer, 2008; Davis et al., 2009; Edwards et al., 2011; Emerson & Moyer, 2002; Emerson et al., 2007, 2017; McAllister et al., 2019). The best known of this group is *Mariprofundus ferrooxydans*, which has a bean-shaped cell that secretes stalks of organic-encased ferrihydrite, which precipitates as a waste product from its metabolic activity (Figure 1). The stalks are usually twisted, but sometimes this trait is not present in the stalks of the PV-1 type strain (Chan et al., 2011, figure S1). These stalks can then serve as a substrate for further iron oxyhydroxide

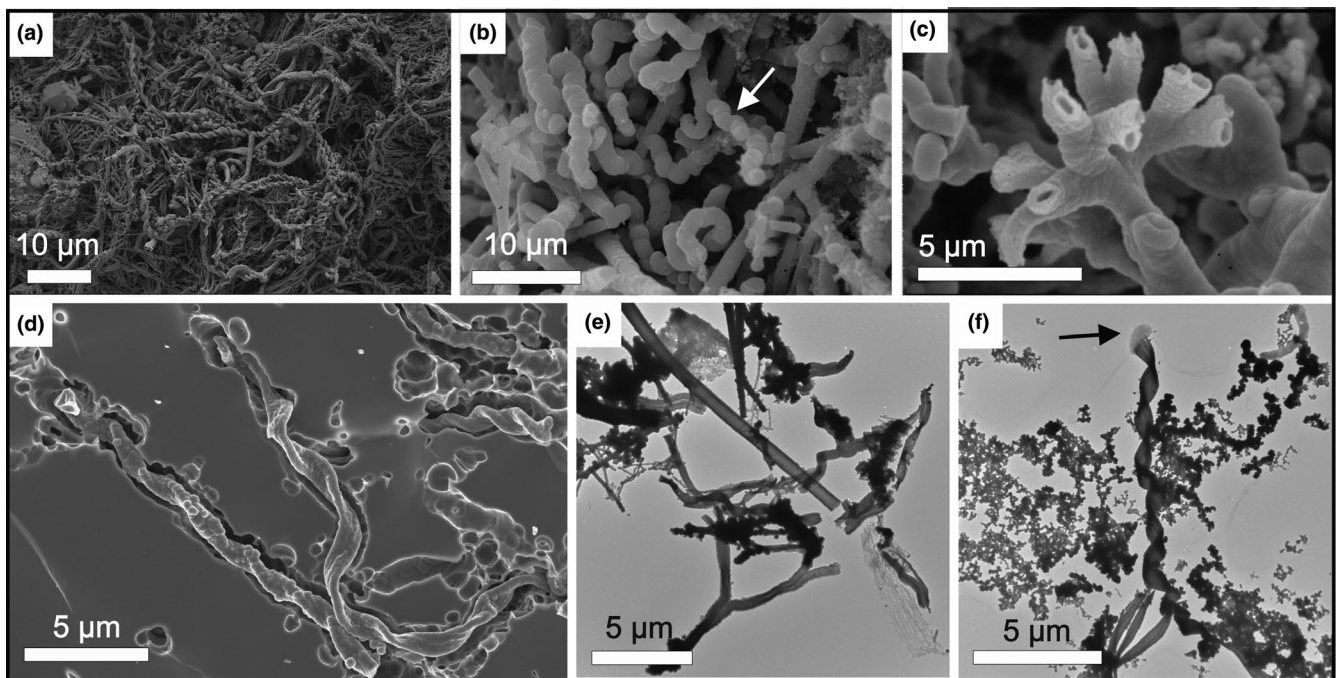


**FIGURE 1** FeOB structures from modern low-temperature hydrothermal vent sites. (a-d) Scanning electron microscope (SEM) images of siliceous ferrihydrite-coated filaments from Troll Wall vent field, Mohns Ridge. (a) Mat of tubular filaments and variably twisted filaments, with straight to curved morphologies; some parallel aligned. (b) Variably twisted filaments; white arrow points to highly twisted example. (c) Highly branched hollow filaments. (d) Twisted filaments enclosed in silica matrix. (e) TEM image of filaments from Loihi Seamount microbial mats showing a variety of morphologies, including cylindrical tubes, twisted stalks, and highly branching filaments. (f) TEM image of cell (black arrow) and twisted stalk of cultured *Mariprofundus ferrooxydans* PV-1 strain, together with Fe-oxide particles

precipitation, increasing the overall Fe/C ratio of the aging stalks, and also causing them to thicken, obscuring some of the fine details, like twisting (Chan et al., 2011; Chan, McAllister, et al., 2016, figure 5C, 7F). At regular intervals, *M. ferrooxydans* cells detach from the stalks and swim actively away to form new stalks elsewhere. *M. ferrooxydans* lives at the narrow interface between the anoxic Fe-rich vent fluid and ambient, oxygenated seawater (Edwards et al., 2011; Glazer & Rouxel, 2009). In culture, the PV-1 strain requires neutral pH and microaerobic conditions, producing stalks at 2.7 to 28  $\mu\text{M O}_2$  (Krepski et al., 2013), with Fe(II) used as an electron donor (Emerson et al., 2007). The stalks of *M. ferrooxydans* are 0.6 to 2.2  $\mu\text{m}$  wide and can bifurcate, as a result of cell division (Figure 1). The stalks typically occur in parallel, a result of coordinated growth of cells following a chemical gradient (Chan, McAllister, et al., 2016). In addition to *M. ferrooxydans*, in natural samples from low-temperature Fe-oxide deposits other Zetaproteobacteria are present, forming different structures. These include unbranching cylindrical sheaths ca. 1  $\mu\text{m}$  in diameter and hundreds of microns long (Fleming et al., 2013), and Y-shaped tubes ca. 2 to 4  $\mu\text{m}$  in diameter and ca. 5 to 50  $\mu\text{m}$  long (Chan, McAllister, et al., 2016; Emerson et al. 2017; Peng et al., 2015). The latter are stalk structures formed by apical cells, similar to the way *M. ferrooxydans* forms its stalks, but these are shorter than *M. ferrooxydans* stalks and are hollow (Chan, McAllister, et al., 2016; Emerson et al. 2017; Peng et al., 2015). Although the organisms that form sheaths and Y-shaped tubes have not been isolated, genomic analyses of major Zetaproteobacteria taxa (cultured and uncultured) show that all Zetaproteobacteria are aerobic iron oxidizers (McAllister et al., 2020). Zetaproteobacteria co-occur with other micro-organisms at low-temperature vents to collectively form mat-like structures on the seafloor (e.g., Chan, McAllister, et al., 2016; Johannessen et al., 2017; Vander Roost et al., 2017, 2018) that are

partially organic and partially mineralogical, and are often associated with amorphous silica (e.g., Rouxel et al., 2018). However, the main framework of these mats is formed by the Zetaproteobacteria (Figure 1). Importantly, the extracellular stalks and sheaths produced by modern FeOB contain only minor amounts of organic carbon (e.g., 0.3 wt% TOC; Laufer et al., 2017), being Fe-oxide waste products rather than cells (Bennett et al., 2014; Chan et al., 2011; Emerson & Revsbech, 1994).

The Phanerozoic contains many examples of marine hydrothermal vent deposits, termed Volcanogenic Massive Sulfides (VMS), from a wide variety of tectonic settings (e.g., Hannington, 2014; Huston et al., 2010). Some of these VMS deposits are closely associated with layers or lenses of jasper (hematite-silica rocks), which in many cases can be traced along strike laterally for hundreds of meters to locally several kilometers (e.g., Duhig et al., 1992; Grenne & Slack, 2003, 2005; Juniper & Fouquet, 1988; Little et al., 2004). Jasper occurrences without lateral continuity may be analogues for the isolated, Si-Fe-oxyhydroxides forming at modern, low-temperature, Fe-rich, and sulfide-poor vents. Many of these Phanerozoic jaspers contain filamentous structures, hundreds of micrometers in length and 5 to 30  $\mu\text{m}$  in diameter, composed of hematite within a microcrystalline quartz matrix (Little et al., 2004 and references therein). The filaments display a variety of morphologies including branching and coiled structures, and dendrites. It has been suggested that these filaments are fossils of FeOB (e.g., Emerson & Moyer, 2002; Little et al., 2004 and references therein; Chan, Emerson, et al., 2016); however, none has yet convincingly been shown to display the characteristic twisted stalks formed by *Mariprofundus ferrooxydans*.

Further back in geological time, VMS deposits as old as 3.5 Ga are known (Huston et al., 2010). Some of these Precambrian VMS are associated with small-scale jaspers and iron formations (Fe-oxides that

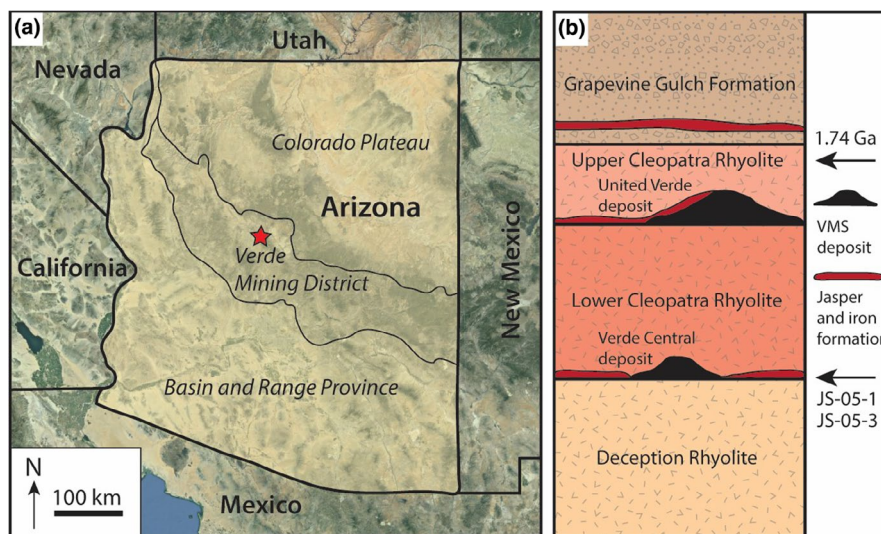


**FIGURE 2** (a) Location of Verde mining district in central Arizona. (b) Simplified stratigraphic section of the VMS-hosting Paleoproterozoic volcanic sequence in northern part of the mining district (modified from Slack et al., 2007), showing stratigraphic positions of VMS deposits, jaspers, and iron formations. Not shown is a stratigraphically lower horizon of jasper and iron formation, in the southern part of the district, between the Shea Basalt and overlying Deception Rhyolite. Total thickness of section varies from 1 to 2.5 km. Note that thicknesses of VMS deposits, jasper units, and iron formations are exaggerated. Stratigraphic levels of samples JS-05-1, JS-05-3, and that used for U-Pb zircon age of 1.74 Ga (Slack et al., 2007) are indicated

lack abundant silica). Such Fe-rich and Si-poor seafloor-hydrothermal deposits, together with jaspers and other VMS-related hydrothermal chemical precipitates, are termed exhalites (e.g., Slack, 2012; Spry et al., 2000). Iron-rich exhalites are similar in some respects to volcanic-hosted, deep-water, Algoma-type Banded Iron Formation (BIF), but differ in being proximal to VMS deposits. In contrast, the generally larger Superior-type BIFs formed in sedimentary basins at shallow-water depths, as shown by the presence of local stromatolites and other sedimentary features (e.g., Bekker et al., 2010; Konhauser et al., 2017).

One example of Precambrian VMS deposits with associated Fe-rich exhalites is in the Jerome area of the Verde mining district in central Arizona, USA (Figure 2a; Lindberg, 2008). Here occur several Cu-rich VMS deposits with associated bedded jaspers and tuffaceous rocks with local rip-up clasts of jasper at the same stratigraphic levels (Slack et al., 2007; Figures 2b and 3a,c,d). Jaspers also occur interlayered with hematite iron formation at a higher stratigraphic level in the Grapevine Gulch Formation, but without associated VMS deposits (Figures 2b and 3b). The VMS deposits in the district are hosted by a thick succession of late Paleoproterozoic (1.74 Ga) rhyolites. This succession lacks evidence of a terrigenous siliciclastic component, suggesting formation within an intraoceanic island arc distal from any continental margin (Anderson, 1989). Occurrence in the district of geographically widespread rhyolite tuffs and cauldron ring fractures implies that the VMS mineralization

took place in a submarine volcanic caldera (Lindberg, 2008). These and other geologic features led Briggs (2018) to propose the Izu-Bonin–Mariana Arc in the South Pacific as a modern analogue. The host volcanic rocks and the VMS deposits were subjected to polyphase deformation and lower greenschist-facies metamorphism during the Paleoproterozoic (Gustin, 1990; Lindberg, 2008). Water depth during formation of the Verde mining district VMS deposits was inferred by Slack et al. (2007) to be  $\geq 850$  m, based on the Cu-rich nature of the ores and a related fluid temperature of  $>300^\circ\text{C}$  required to transport appreciable Cu in solution (e.g., Hannington et al., 1995), together with the hydrostatic pressure needed for stabilization of aqueous Cu in seafloor-hydrothermal fluids having near-seawater salinities. Using more recent data in Hannington (2014), however, a minimum water depth of 500 m is adopted here with a revised formational temperature of  $\geq 265^\circ\text{C}$  for depositing the Cu-rich mineralization in the district.

From mineralogical and geochemical studies of the jaspers in the Jerome area, Slack et al. (2007) inferred that late Paleoproterozoic deep seawater was in a transitional, suboxic state that allowed the oxidation of hydrothermal  $\text{Fe}^{2+}$  to  $\text{Fe}^{3+}$ , which in their model was preserved in hematite within the jaspers. This inference is at odds with many (but not all, e.g., Ohmoto et al., 2006; Planavsky et al., 2018; Slack et al., 2009; Sperling et al., 2014) reconstructions of Proterozoic seawater redox states, derived largely from geochemical studies of shales in marine sedimentary sequences



**FIGURE 3** (a) Field photograph of orange and red jasper layers and intervening rhyolite tuff (dark-gray) containing angular jasper clasts, from lowermost part of lower Cleopatra Rhyolite (Figure 2b). Upper red jasper layer is near base of outcrop that contains sample JS-05-1. Sample JS-05-03 was collected ca. 20 m along strike from this outcrop. Hammer is 40 cm long. (b) Field photograph of folded layers of jasper and hematite iron formation (dark), from lower part of Grapevine Gulch Formation (Figure 2b). Coin is 2.1 cm in diameter. (c) Field photograph of angular jasper and chert rip-up clasts in crystal-rich rhyolite tuff. Note dark-gray rim on elongated jasper clast and completely bleached jasper clast to the left, caused by variable diagenetic reduction in ferric to ferrous iron during sediment burial. Knife is 8.9 cm long. (d) Field photograph of angular jasper rip-up clasts in rhyolite lapilli tuff, enclosed by massive rhyolite tuff. Note lack of hematite in matrix of lapilli tuff. Coin is 2.1 cm in diameter

(e.g., Canfield, 1998; Bekker et al., 2004; Poulton et al., 2004; Canfield, 2005; Canfield et al., 2008; Meyer & Kump, 2008; Kendall et al., 2009; Poulton et al., 2010; Poulton & Canfield, 2011; Planavsky et al., 2011; Reinhard et al., 2013), which suggest that either ferruginous or euxinic conditions prevailed in the deep sea during this long time period between 1.8 and 0.8 Ga (the so-called "Boring Billion"). Light microscope investigations of the Jerome area jaspers revealed in some samples distinctive hematitic filaments, described briefly by Slack et al. (2007). Herein, we present a detailed investigation of these filaments using a variety of techniques, in order to fully elucidate their morphology and formation. Based on the new information and by comparison with Phanerozoic jasper filaments and modern FeOB, we interpret the Jerome area filaments as having a biological origin and suggest these are fossil products of benthic, microaerobic, FeOB that lived at low-temperature hydrothermal vents. We further discuss the implications of this interpretation for the redox state of late Paleoproterozoic deep seawater, and the deposition of Precambrian iron formations.

## 2 | MATERIAL AND METHODS

### 2.1 | Optical and scanning electron microscopy

Details of collection of the Jerome area jaspers, together with background geology and related whole-rock geochemical data, are given in Slack et al. (2007). The studied materials come from a 1-m-thick jasper layer that occurs at the same stratigraphic level as the small Verde Central VMS deposit ca. 160 m to the south (Slack et al., 2007; Figures 2 and 3a). Hereafter, we refer to this layer as the Verde Central jasper (VCJ). VCJ samples JS-05-1 and JS-05-3 were used in this study for detailed investigation. Filamentous structures within these samples were identified initially in polished thin sections (100 or 200  $\mu\text{m}$  thick) using a Leica DM750P petrographic microscope under plane and crossed polarized light, fitted with a Leica DFC290HD digital camera. One thin section from VCJ JS-05-3 was used to obtain digital measurements of the filaments via Leica Application Suite v.3.7.0. Two thin sections from VCJ JS-05-1 were prepared with 14-nm-thick carbon coats and examined by scanning electron microscopy (SEM) and backscattered electron (BSE) imaging at 10 keV, using a FEI Quanta 650 FEG-ESEM with an Oxford X-max 80 SDD Energy Dispersive Spectrometer (EDS) at the Leeds Electron Microscopy and Spectroscopy Centre, University of Leeds, UK.

### 2.2 | Raman spectroscopy

One thin section (200  $\mu\text{m}$  thick) from VCJ sample JS-05-3 was analyzed at the Department of Geological Sciences, Stockholm University, Sweden, using a confocal laser Raman microspectrometer (Horiba instrument LabRAM HR 800; Horiba Jobin Yvon, Villeneuve d'Ascq, France), equipped with a multichannel, air-cooled

( $-70^{\circ}\text{C}$ ),  $1,024 \times 256$  pixel CCD (charge-coupled device) detector. Acquisitions were obtained with an 1,800 lines/mm grating. Excitation was provided by an Ar-ion laser ( $\lambda = 514$  nm) source. Spectra were recorded using a low laser power of 0.1–1 mW at the sample surface to avoid laser-induced degradation. Sampling was carried out using an Olympus BX41 microscope coupled to the instrument; the laser beam was focused through a 100 $\times$  objective to obtain a spot size of ca. 1 mm. The spectral resolution was  $\sim 0.3$   $\text{cm}^{-1}$  pixel $^{-1}$ . Typical exposure time was 10 s with 10 accumulations. The accuracy of the instrument was controlled by repeated use of a silicon wafer calibration standard with a characteristic Raman line at  $520.7$   $\text{cm}^{-1}$ .

### 2.3 | Synchrotron-based X-ray tomographic microscopy (SRXTM)

SRXTM was carried out at the X02DA (TOMCAT) beamline (Stampanoni et al., 2006) at the Swiss Light Source, Paul Scherrer Institute, Villigen, Switzerland. The figured sample was broken out from a  $\sim 200$ - $\mu\text{m}$ -thick, double-polished section from VCJ sample JS-05-3 and glued to a brass pin. It was then scanned at a beam energy of 20 keV. Transmitted radiation was converted to visible light using a 20- $\mu\text{m}$ -thick LAG:Ce scintillator or a 5.9- $\mu\text{m}$ -thick LSO:Tb scintillator. The image was magnified with 10 $\times$ , 20 $\times$ , or 40 $\times$  microscope objectives and digitized by a sCMOS camera (PCO.edge). The resulting voxel size was 0.65  $\mu\text{m}$  for the 10 $\times$ , 0.325  $\mu\text{m}$  for the 20 $\times$ , and 0.1625  $\mu\text{m}$  for the 40 $\times$  objective. For each scan, 1,501 to 2,001 projections equiangularly spaced over  $180^{\circ}$  were acquired, with exposure times of 220 to 800 ms per single projection. Tomographic reconstruction was done using a highly optimized algorithm based on the Fourier method (Marone & Stampanoni, 2012), and the obtained tomographic volumes were visualized and rendered using Avizo software (Thermo Fisher Scientific).

### 2.4 | Focused ion beam-transmission electron microscopy (FIB-TEM)

Another thin section (200  $\mu\text{m}$  thick) from VCJ sample JS-05-3 was analyzed using FIB-TEM. Potential target filaments for FIB were identified optically using a Nikon Eclipse LV100 polarizing microscope at the University of Bergen, Norway. The slide was then coated with a 30-nm-thick layer of Au, and locations of individual microfossils were confirmed by SEM using a Zeiss Supra 55VP SEM, also at the University of Bergen. For easy recognition of the FIB-TEM target filaments, only horizontally oriented specimens that intersected the surface of the section were selected.

Three ultrathin filament cross sections were prepared from the slide using a FEI Helios NanoLab 600 DualBeam FIB-SEM at the NTNU NanoLab in Trondheim, Norway. The target areas were identified and monitored with a FEG-SEM, while milling was performed with a focused  $\text{Ga}^{+}$  ion beam. A Pt protection layer

**TABLE 1** Whole-rock analyses of jaspers from the Verde Central horizon

Sample No.	JS-05-1	JS-05-2	JS-05-3	JS-05-3 BEK	JS-05-4
SiO <sub>2</sub> (wt %)	94.47	96.15	94.24	89.51	95.34
Al <sub>2</sub> O <sub>3</sub>	0.30	0.74	0.17	0.20	0.38
Fe <sub>2</sub> O <sub>3</sub>	3.08	1.44	3.41	7.78	0.65
FeO	1.13	1.07	0.96	1.21	2.14
MnO	0.004	0.011	0.018	0.005	0.010
MgO	0.02	0.02	0.03	0.04	0.17
CaO	0.02	0.03	0.03	0.06	0.02
Na <sub>2</sub> O	0.08	0.08	0.07	0.09	0.06
K <sub>2</sub> O	0.07	0.04	0.07	0.06	0.06
TiO <sub>2</sub>	0.010	0.016	0.007	0.016	0.007
P <sub>2</sub> O <sub>5</sub>	<0.01	<0.01	<0.01	<0.01	0.05
LOI	0.51	0.46	0.66	0.55	0.62
Total	99.68	100.05	99.63	99.50	99.53
Be (ppm)	<1	<1	<1	<1	<1
Br	<0.5	0.5	<0.5	<0.5	0.5
Ga	<1	1	<1	<1	1
Ge	1.0	1.1	0.7	0.7	0.9
Sc	0.6	0.7	0.3	0.3	1.9
V	<5	<5	<5	<5	<5
Cr	9	29	13	459	94
Nb	0.7	0.9	0.9	0.5	1.3
Ta	<0.01	<0.01	<0.01	0.10	<0.01
Zr	7	7	7	5	22
Hf	0.1	0.2	<0.1	<0.1	0.2
Th	0.11	0.18	0.05	0.08	0.06
U	0.36	0.32	0.25	0.19	0.53
Ni	4	12	4	13	10
Cu	7	27	4	9	13
Pb	4	<3	<3	<3	<3
Zn	21	24	5	4	19
Cd	0.3	<0.3	<0.3	0.5	0.4
Ag	<0.3	<0.3	<0.3	<0.3	<0.3
Au (ppb)	69	55	32	<2	14
As	5.5	6.3	3.5	3.8	10.8
Sb	0.72	0.96	0.48	0.48	1.04
Se	<3	<3	<3	<3	<3
Mo	<2	3	<2	10	<2
Sn	<1	<1	<1	<1	<1
W	1.2	0.7	1.0	1.4	0.9
Tl	<0.05	<0.05	<0.05	<0.05	<0.05
Bi	0.6	0.2	0.3	<0.1	0.4
In	<0.1	<0.1	<0.1	<0.1	<0.1
Ir	<5	<5	<5	<5	<5
Cs	<0.1	<0.1	<0.1	<0.1	<0.1
Rb	<1	<1	<1	<1	<1

(Continues)

TABLE 1 (Continued)

Sample No.	JS-05-1	JS-05-2	JS-05-3	JS-05-3 BEK	JS-05-4
Sr	12	18	<2	3	2
Ba	10	9	9	6	6
Y	34.2	79.4	31.0	3.76	251
La	1.24	2.53	0.73	0.36	1.79
Ce	2.52	5.09	1.56	0.76	4.36
Pr	0.36	0.68	0.22	0.10	0.59
Nd	1.86	3.63	1.24	0.49	3.88
Sm	0.58	1.23	0.44	0.14	2.16
Eu	0.149	0.330	0.119	0.036	0.861
Gd	1.20	3.19	1.04	0.22	7.29
Tb	0.31	0.82	0.30	0.05	2.12
Dy	2.65	6.70	2.50	0.39	18.7
Ho	0.70	1.74	0.67	0.10	5.34
Er	2.48	6.29	2.50	0.36	20.4
Tm	0.431	1.095	0.442	0.062	3.670
Yb	3.13	8.02	3.23	0.46	26.4
Lu	0.514	1.367	0.524	0.076	4.325
La/Yb	0.396	0.315	0.226	0.787	0.068
La <sub>SN</sub> /Yb <sub>SN</sub>	0.029	0.023	0.017	0.058	0.005
Ce/Ce*	0.87	0.90	0.90	0.92	0.98
Eu/Eu*	0.84	0.78	0.83	0.97	1.02

Note: REE anomalies are calculated by shale normalization (SN) using data for average Post-Archean Australian Shale (PAAS; Taylor & McLennan, 1985):  $Ce/Ce_{SN}^* = Ce_{SN} / \sqrt{(La_{SN} \times Pr_{SN})}$ ;  $Eu/Eu_{SN}^* = Eu_{SN} / \sqrt{(Sm_{SN} \times Gd_{SN})}$ .

was deposited on the surface of the target cross section prior to FIB milling. The first part of the protection layer was deposited by electron beam-assisted deposition to avoid ion beam damage into the subsurface of the sample. Each lamella was transferred to dedicated Cu half-grids for TEM by standard lift-out-technique. All coarse thinning was performed at 30 kV acceleration voltage for the Ga<sup>+</sup> ions. Final thinning was first performed at 5 kV and then 2 kV acceleration voltage on either side of the lamella to minimize surface damage. The final thickness of the FIB lamellae was ca. 100 nm.

The three FIB foils were analyzed at the TEM Gemini Centre at NTNU in Trondheim using a double Cs-corrected, cold-FEG JEOL ARM 200F, operated at 200 kV. Prior to insertion, the samples were gently plasma cleaned in a gas mixture of 75% Ar and 25% O<sub>2</sub> for 30 s to remove adventitious hydrocarbon contamination. EDS and EELS were done in scanning transmission electron microscopy (STEM) mode. EDS was performed with a 27 mrad beam semi-convergence angle and a beam current of 380 pA. These conditions gave a 1.4 Å spatial resolution, but on amorphous material or on crystals away from high symmetry orientations, the beam diameter quickly increases through the sample due to the large convergence angle of the beam. A 100-mm<sup>2</sup> Centurio detector, covering a solid angle of 0.98 sr, was used for EDS. In

Figure 7 and Figure S2, the pixel size and dwell time in the EDS element maps were 10 nm/0.03 s and 5 nm/0.05 s, respectively, but acquired with 16 × 16 sub-pixel scanning to avoid severe beam damage. The beam dose during STEM-EDS was 7,000 e/Å<sup>2</sup> in Figure 7 and ca. 45,000 e/Å<sup>2</sup> in Figure S2. The EDS maps were processed in MATLAB using the jet color scale with matrix values from 0 (dark blue) to 255 (dark red). EELS was performed with a GIF Quantum ER, operated in dual-EELS mode. A 110 pA beam current and 27 mrad semi-convergence angle were combined with a 33 mrad collection semi-angle into the GIF. An energy dispersion of 0.025 eV/channel gave an energy resolution of 0.50 eV as determined from the full width at half maximum of the zero-loss peak (ZLP). The energy scale of the core-loss spectra was calibrated from the position of the ZLP in the low-loss spectra. The EEL spectra in Figure S1 were acquired while the beam was quickly scanned (512 × 512 pixels with 2 μs pixel time and 0.5 s frame time) over a ca. 100 nm × 100 nm region, giving a fluence rate of 690 e/(Å<sup>2</sup>s). The acquisition time for the Fe L<sub>2,3</sub> spectra was 5 s, exposing the sample to a total beam dose of 3,430 e/Å<sup>2</sup>. The chemical shift method (e.g., Tan et al., 2012) was used in combination with the ratio and distance between the L<sub>3</sub> and L<sub>2</sub> peaks to determine the oxidation state of Fe in poorly crystalline material. Hematite grains identified by diffraction were used as a reference for Fe<sup>3+</sup>.

## 2.5 | Whole-rock geochemistry

Five jasper samples from the Verde Central horizon (Figure 2b) were analyzed for major, trace, and rare earth elements (REE) in a commercial laboratory by fusion-based ICP-MS methods as described in Slack et al. (2007). Details of the analytical methods, including accuracy and precision, are available at [www.actlabs.com](http://www.actlabs.com). Analyses of these five samples, which have not been reported previously, are listed in Table 1.

## 2.6 | Comparative modern material

Material from modern, low-temperature hydrothermal vent areas at Troll Wall on Mohns Ridge, Norwegian-Greenland Sea, and on Lō'ihi Seamount, off-shore Hawaii, was used for comparison with the VCJ filaments (Figure 1). For collection and imaging details of the modern material, see Pedersen et al. (2010) and Glazer and Rouxel (2009), respectively.

# 3 | RESULTS

## 3.1 | Filament occurrence, morphologies, and mineralogical composition

Filaments in the VCJ samples occur in millimeter-scale domains bounded by multiple cross-cutting quartz veins and areas of variably sized quartz grains with greater or lesser quantities of disseminated hematite crystals (Figure 4a-c, Figure 5a). Within the studied samples, the area of filament-rich domains is small (<5%) relative to the overall rock volume. The filaments within the domains are enclosed by equigranular quartz grains 5 to 40  $\mu\text{m}$  in diameter having triple-junction and slightly curved to straight grain boundaries (Figure 4c-f, Figure 6c); many filaments continue across grain boundaries (Figure 4c,f), thus demonstrating they are not grain-boundary artifacts. In addition to the filaments, the quartz grains enclose scattered, micrometer-scale hematite crystals with variable shapes (Figures 4a,d and 6b).

Filament diameters vary between 0.9 and 4.7  $\mu\text{m}$  (mean 2.5  $\mu\text{m}$ ;  $n = 43$ ) in VCJ sample JS-05-1 (measured using binocular microscope) and between 2.3 and 12.4  $\mu\text{m}$  in VCJ sample JS-05-3 (based on tomographic volume renderings in Figure 5a-c). In general, the filaments have constant diameters along their length, apart from places where branches exist. The longest traceable filaments are 120  $\mu\text{m}$  in length (Figure 5a), although this can be regarded as a minimum value because the longest examples cross the plane of the petrographic thin sections. The filaments form densely to loosely packed meshworks (Figures 4a-c and 5). In some places, the filaments are roughly parallel to each other, forming bundles of >10 individuals (Figure 5a,b). Individual filaments have sinuous to curved shapes; a few are tightly coiled (Figure 5a,c). Several filaments show possible twisted shapes (Figure 4b,d),

and many display irregular branching patterns and bifurcations (Figures 4a,e,f, and 5d).

The filaments are quartz-filled cylinders with walls formed of hematite crystals as documented by TEM diffraction and Raman spectroscopy (Figures 4d-f, 6b, and 7a; Figure S1). Thicknesses of the walls vary but are typically less than 1  $\mu\text{m}$ . In many filaments, the hematite crystals forming the walls are so sparse that they do not touch each other (Figure 7a). TEM of two filaments shows the hematite crystals that form walls have a blocky shape and are 0.2 to 0.5  $\mu\text{m}$  along the long axes (Figure 7b). An additional Si-Fe phase is present in one of the cross sections (Figure 7b). This phase displays a locally ordered microstructure but lacks long-range crystallographic order and therefore gives a diffuse, circular diffraction pattern characteristic of poorly crystalline material (Figure S1). Silicon content is significantly higher in the poorly crystalline phase than in the hematite crystals, and the content of iron is lower (Figure 7c-e). The poorly crystalline phase and the hematite reference grains show identical chemical shifts, Fe L3/L2 ratios, and distances between L3 and L2 peaks in the EELS spectra, thus indicating that the oxidation state of Fe in the poorly crystalline material is +3. There is no carbon present in the two filaments investigated using TEM (Figure 7f), and we did not find the characteristic D and G bands of the ordering of organic carbon in our Raman investigation. However, very small amounts of carbon occur in the third TEM section, which did not transect an obvious filament (Figure S2). Here, the carbon is present in the interface between larger hematite crystals and quartz and has a distinct fibrous habit (not shown).

## 3.2 | Rare earth element geochemistry

Major and trace element data for the VCJ samples are similar to those for the other jaspers analyzed from the Verde mining district (Slack et al., 2007). However, results for REE differ significantly in terms of abundances and especially shale-normalized patterns (Figure 8a). Relative to jaspers from the United Verde and Copper Chief horizons (Figure 2b), the VCJ samples display mostly higher REE abundances, with strong enrichments particularly in the heavy rare earth elements (HREE) and consequently very low ratios of light rare earth elements (LREE) to HREE ( $\text{La}_{\text{SN}}/\text{Yb}_{\text{SN}} = 0.005\text{--}0.058$ ; Table 1). All five analyzed VCJ samples have very small negative or no Eu anomalies ( $\text{Eu}/\text{Eu}^* 0.78\text{--}1.02$ ) using the geometric mean calculation method of Taylor and McLennan (1985). This same method yields uniformly small negative Ce anomalies ( $\text{Ce}/\text{Ce}^* 0.87\text{--}0.98$ ). However, the scheme of Lawrence and Kamber (2006), which does not rely on La data because of the common presence of positive La anomalies in marine sediments, yields uniformly small to moderate positive Ce anomalies (1.14–1.48) but these values are likely overestimated by as much as 20% (cf. Kamber et al., 2014). The largest Ce anomaly of 1.48, determined using this latter scheme, exceeds the value of 1.3 proposed by Tostevin et al. (2016) as

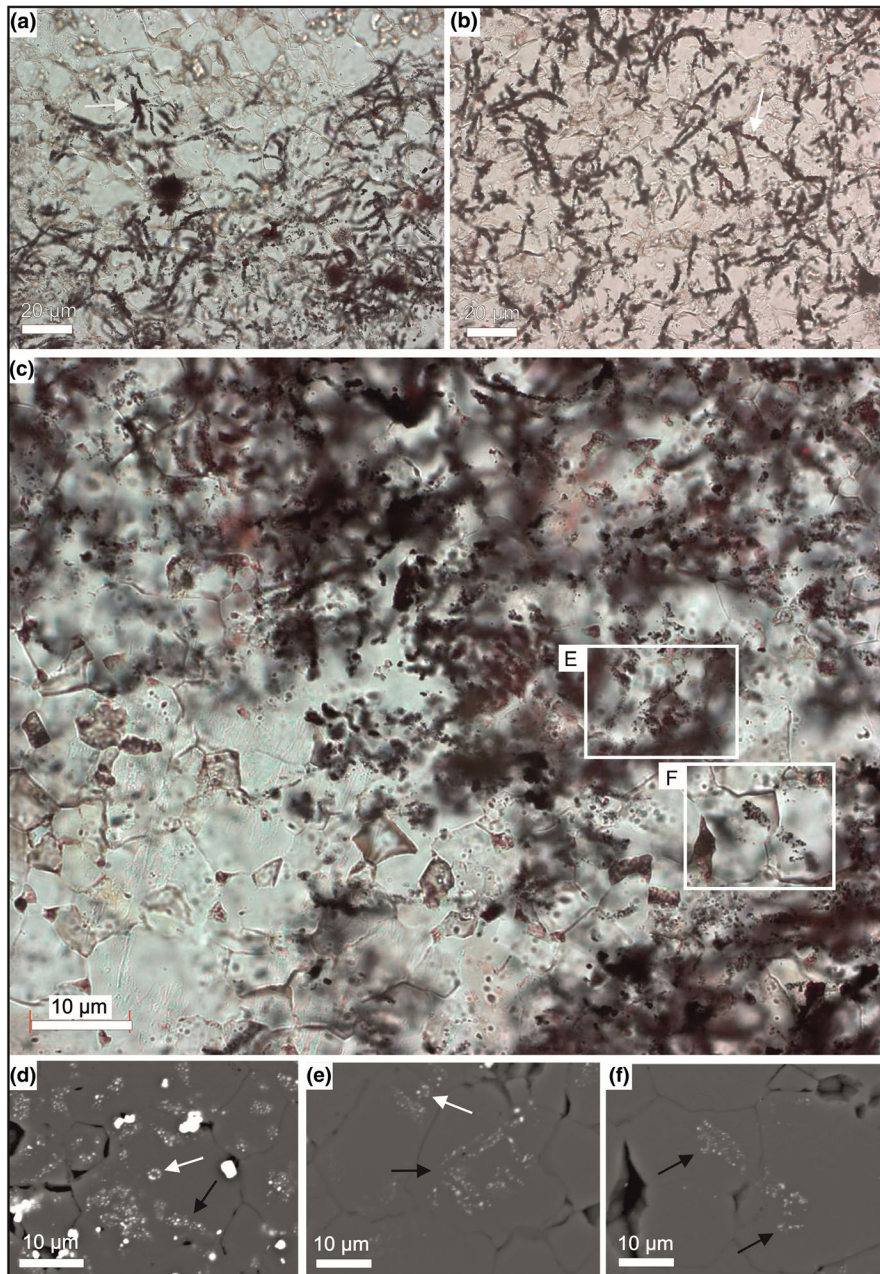


**FIGURE 4** Hematite filaments from Verde Central jasper sample JS-05-1. (a-c) Photomicrographs in plane-polarized light of branching (white arrow in A) and putative twisted filaments (white arrow in b); insets in (c) show detailed areas (e,f). (d-f) Scanning electron microscope-backscattered electron (SEM-BSE) images of filaments, showing branching (black arrows in e,f) and putative twisted (black arrow in d) forms. White arrows in (d) and (e) show filaments in transverse section. (c) and (f) show a filament that transgresses quartz grain boundaries (c,f)

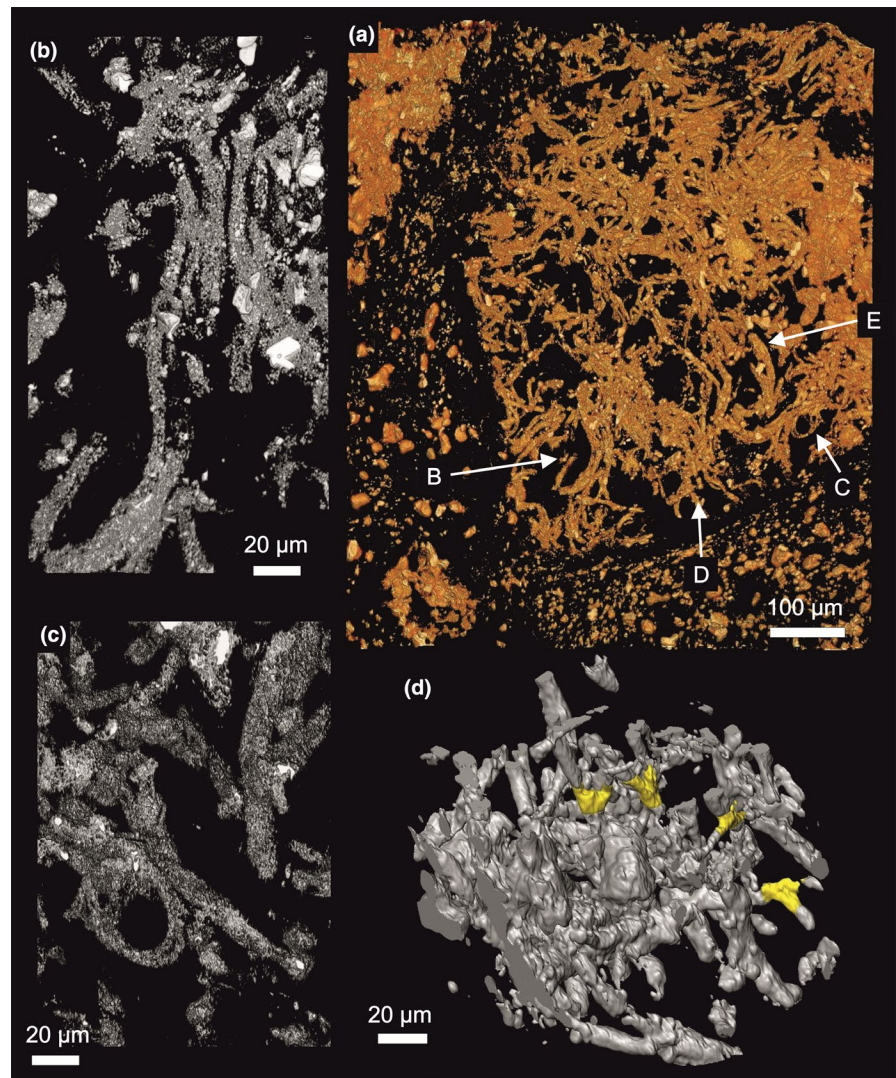
a minimum to define true positive Ce anomalies, but the use of this scheme is questionable because it relies on a linear projection of Sm-Nd-Pr to Ce, which is not applicable to the VCJ samples that display highly curved trends for PAAS-normalized LREE (Figure 8a). We therefore take a conservative approach and suggest that the five VCJ samples lack significant Ce anomalies, either negative or positive.

In contrast, jaspers from the United Verde and Copper Chief horizons (e.g., JS-05-37, JS-05-39) have either no, or small positive or negative, Ce anomalies and small to moderate positive Eu anomalies. Low-silica iron formation samples in the district (lower Grapevine Gulch Formation; Figure 2b) show higher REE abundances, higher LREE/HREE ratios, and small positive Ce and Eu anomalies (Figure 8a). For comparison, the rhyolitic host rocks display high REE

abundances, low LREE/HREE ratios, and small to moderate negative Eu anomalies (Figure 8b).

REE data for representative examples of modern Fe-Si oxyhydroxide deposits show a large range in abundances and LREE/HREE ratios, with small negative Ce anomalies and small to moderate positive Eu anomalies (Figure 8c). However, none of these modern Fe-Si samples has the extremely low LREE/HREE ratios that characterize the VCJ samples. In terms of modern fluids, only waters from Mono Lake in California display a similar LREE/HREE ratio with relatively flat HREE abundances; typical seawater and some modern, low-Fe marine pore fluids have slightly higher ratios (Figure 8d). Importantly, fluids from modern submarine-hydrothermal vents also differ greatly in having large positive Eu anomalies that reflect reduced, high-temperature (>300°C) conditions (e.g., Mills & Elderfield, 1995).

**FIGURE 5** Synchrotron-based X-ray tomographic microscopy volume (a–c) and surface (d) renderings of hematite filaments from Verde Central jasper sample JS-05-3. (a) shows sharply delimited area with dense filaments. Insets show filaments with parallel bundles (b), with looped morphology (c), and those with branches highlighted in yellow in (d). White arrow E indicates the filament from which Raman spectra were obtained (Figure 6). For stereo anaglyph of 5c, see Figure S3. For 3-D animations of 5a,b, and d, see Video S1-S3



## 4 | INTERPRETATION AND DISCUSSION

### 4.1 | Biogenicity of VCJ filaments

The VCJ filaments conform to the majority of established biogenicity criteria for documenting Precambrian microfossils (Buick, 1990; Cady et al., 2003). These criteria include the following: (a) being intrinsic to the rock and pre-dating quartz crystallization (probably from an original silica gel; see Grenne & Slack, 2003) and subsequent quartz veining; (b) having a narrow range of diameters that generally do not vary longitudinally, and that are within the size range of modern micro-organisms; (c) co-existing with other filaments of similar morphology; and (d) occurring in a paleoenvironment analogous to those where bacteria grow today (see below). The only biogenicity criterion of Buick (1990) not satisfied by the VCJ filaments is their apparent lack of organic matter (e.g., kerogen). The weak EDS carbon signal we found in one of the FIB-TEM sections (Figure S2) is not spatially associated with a well-defined filament, and its origin could have several explanations, including being contemporaneous to filament formation, or a later contamination related to diagenesis or

metamorphism. However, we emphasize that the lack of carbon in the studied VCJ filaments does not preclude a biological origin, because the stalks and sheaths produced by modern Zetaproteobacteria contain little organic carbon (<1 wt% TOC; Bennett et al., 2014; Laufer et al., 2017). Further, the cells that create the stalks and sheaths are only loosely attached to these structures and can become easily detached from them, with consequent carbon loss. In addition, any carbon originally present in the VCJ protolith could have been mobilized later, by dissimilatory Fe reduction (Emerson, 2009), or during diagenesis/low-grade metamorphism (Johannessen et al., 2020).

An alternative explanation for the formation of the VCJ filaments is that they are “biomorphs,” that is, abiogenic features that resemble biological structures (e.g., Garcia-Ruiz et al., 2009). In laboratory experiments, McMahon (2019) was able to grow filamentous tubular structures formed of Fe-(oxyhydr)oxides and amorphous hydrated Fe-Si phases, from polycrystalline ferrous sulfate granules placed into aqueous solutions of sodium silicate or sodium carbonate at ambient temperature and pressure. The tubes were of the same scale as the VCJ filaments in terms of diameters, and had some of the same morphologies,

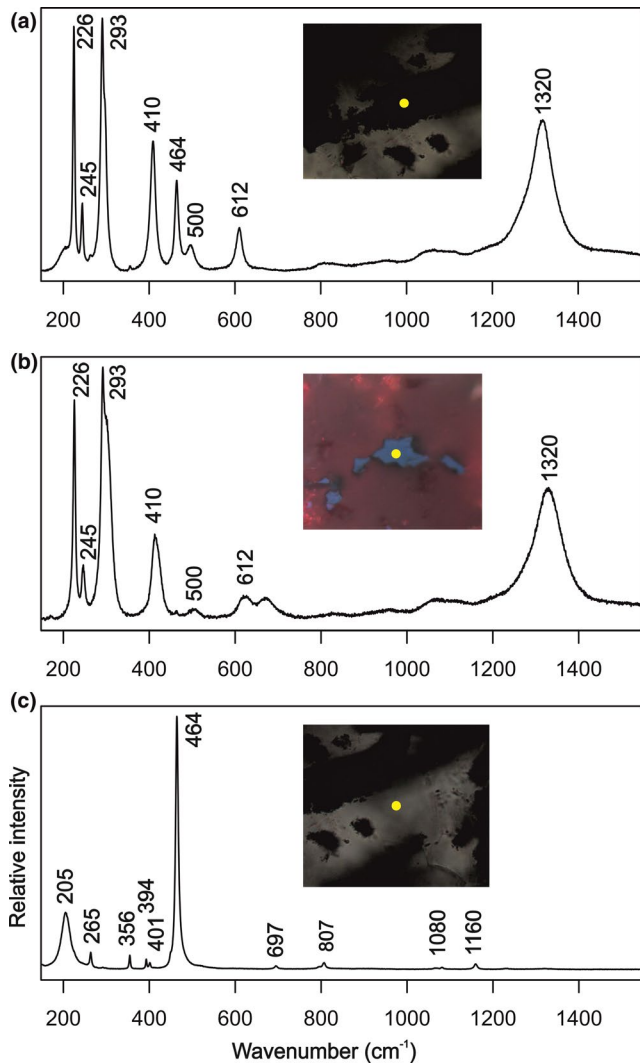


**FIGURE 6** Raman spectra and light microscope images of filament area indicated in Figure 5a. Yellow spots indicate where laser beam was focused for analysis. (a) Hematite spectrum of filament mixed with a peak at  $464\text{ cm}^{-1}$  from surrounding quartz. (b) Hematite spectrum of filament. (c) Quartz spectrum of surrounding mineralogy. Photomicrographs are in transmitted light (a and b), and reflected light (b)

including both straight and strongly curved shapes, and true (non-crystallographic) branching structures. However, there are quite a few differences between the McMahon biomorphs and the VCJ filaments; in particular, the latter commonly form parallel bundles and lack tapering terminations, and do not originate at seed crystal “knobs”. The most obvious difference is that many of the VCJ filaments have walls formed of isolated hematite crystals, and thus cannot be “crystal garden” structures formed of minerals growing on pre-existing minerals. In contrast, all of the biomorphs grown by McMahon (2019) have contiguous mineral walls.

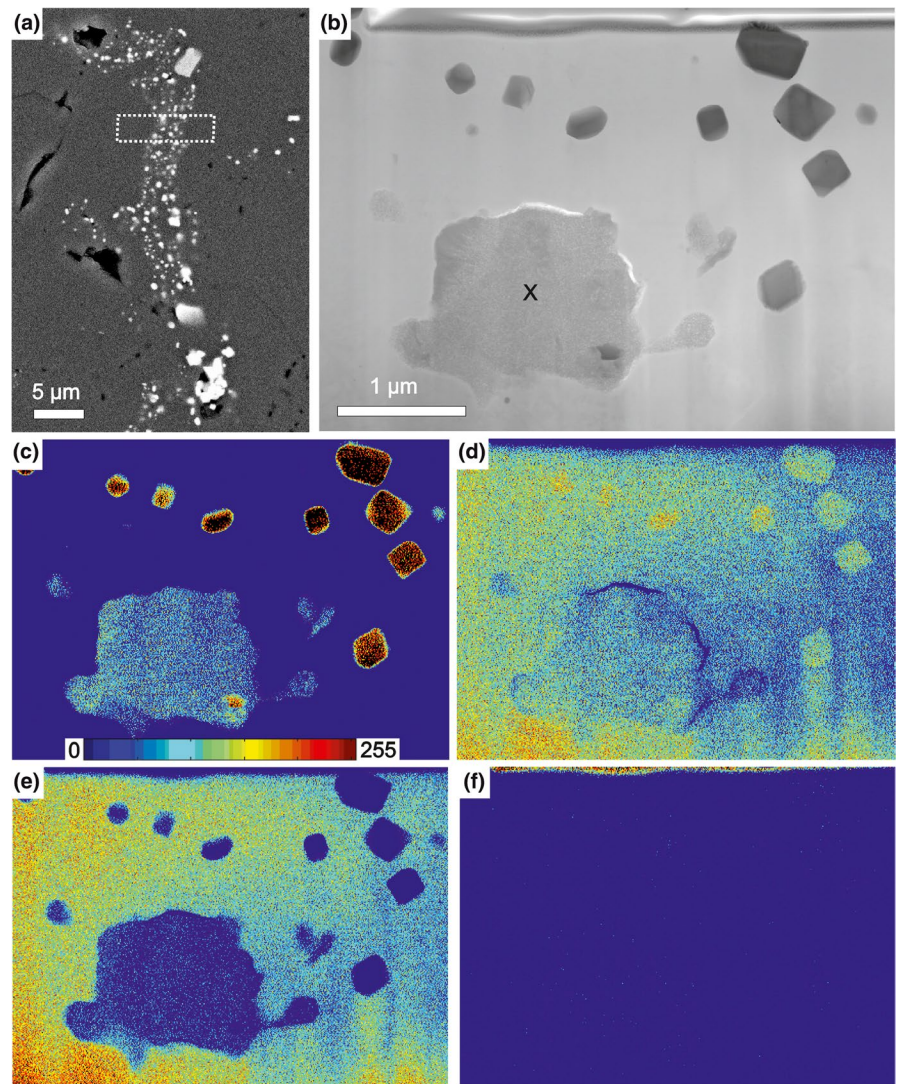
In modern low-temperature marine FeOB mats and Fe-oxide deposits, a wide variety of filamentous and dendritic structures are present (e.g., Hopkinson et al., 1998; Johannessen et al., 2020), which are also seen in Phanerozoic jaspers (e.g., Little et al., 2004).

Johannessen et al. (2020, figure 9) listed five criteria for the identification of biosignatures for Fe-oxidizing bacteria in modern, silicified, low-temperature hydrothermal deposits. The VCJ filaments pass biosignature criteria 3, 4, and 5, because they show sequential bifurcation rather than nodes with multiple branches (criterion 3), have semi-parallel filamentous textures rather than highly directional radial textures (criterion 4), and show dendritic and radial filamentous textures rather than banded dendrites (criterion 5). The VCJ filaments also pass one of the two biosignature criteria for filament construction (criterion 2), in that they are not hollow silica tubes, although the VCJ filaments do have greater diameters than the biogenic filaments of criterion 2. Criterion 1 of Johannessen et al. (2020) is that Fe-oxidizing bacterial filaments have solid cores, whereas abiotic filaments have cores formed of separate spherules. The VCJ filaments lack solid cores, but instead have walls formed of isolated hematite crystals (Figure 7). This discrepancy can be explained by the biogenic filaments in criterion 1 of Johannessen et al. (2020) representing zeta-proteobacterial stalks, rather than zeta-proteobacterial tubes, which have hollow cores and walls formed of iron oxyhydroxides (see Johannessen et al., 2020, figure S3E,F, and Li et al., 2012, figure 3). For these reasons and those given above, we interpret the VCJ filaments as having a biological rather than an abiogenic origin.

## 4.2 | VCJ filaments as FeOB

Using the Uniformitarian principle, the obvious organisms with which to compare the VCJ filaments are Zeta-proteobacteria FeOB from modern, deep-marine, low-temperature hydrothermal vents (Figure 1). Many similarities exist in terms of size and morphology, with filaments forming mesh-like networks (compare Figure 1a,b with Figures 4a,b and 5a), occurring in parallel (compare Figure 1a with Figure 5a,b), and having regular branches (compare Figure 1c,e and Figures 4a,e,f, and 5d). The diameters of the thinnest VCJ filaments in sample JS-05-1 are within the range of modern Zeta-proteobacteria (Figure 1), but the thickest filaments in sample JS-05-3 are around three times as wide. It is possible that a few of the VCJ filaments are twisted (Figure 4b,d), like *Mariprofundus* stalks (Figure 1f), although this is unclear in our samples. Because most of the VCJ filaments are cylindrical, they were probably originally not *Mariprofundus*-like stalks, but rather branching tubular structures, similar to those shown in Figure 1c,e. The comparison with modern FeOB allows us to infer a preservational (i.e., taphonomic) pathway to explain the morphology and mineralogy of the VCJ filaments, and also the metabolism of the micro-organisms that formed them, which has paleoenvironmental implications. We suggest that the VCJ filaments were formed by cells that oxidized reduced iron from vent fluids as an energy source, with iron oxyhydroxides being a product from this reaction. The cells precipitated the resultant iron oxyhydroxides as tubular structures, rather than having minerals forming on the cell surfaces. The VCJ cells would have undergone division at regular intervals to form branched tubes (see Emerson

**FIGURE 7** Focused ion beam-transmission electron microscopy images of hematite filament from Verde Central jasper sample JS-05-3. (a) SEM-BSE image of analyzed filament; inset shows area from which FIB foil was recovered. (b) Brightfield STEM image of FIB foil from (a); X marks poorly crystalline grain. (c-f) EDS maps of B: (c) Fe Ka, (d) O Ka, (e) Si Ka, (f) C Ka



et al., 2017), eventually producing bush-like structures, together appearing as complex meshes. In our model, the cells were growing on the seafloor in mat-like structures, rather than as flocs within buoyant hydrothermal plumes (Slack et al., 2007). Modern marine microaerobic, Fe-oxidizing Zetaproteobacteria can occur in the water column, but the described planktonic strains *Mariprofundus aestuarius* and *M. ferrinatatus* excrete dreadlock-like bundles of poorly crystalline iron oxyhydroxide rods that are significantly shorter and weigh less than the extracellular stalks and sheaths produced by *M. ferrooxydans* and other benthic relatives, and in modern seawater do not accumulate in filamentous microbial mats (Chiu et al., 2017). Further, genomic studies of microbial communities from modern hydrothermal vent plumes have not found Zetaproteobacteria or genes for iron oxidation, but rather show sulfur oxidation is the most important biogeochemical process occurring (Anantharaman et al., 2016). At the VCJ site, iron-rich hydrothermal activity may then have waned and the VCJ cells actively swam away from or dropped off the mineralized tubes, with consequent loss of organic carbon from the VCJ microbial mats. Silica would then have precipitated as an amorphous phase within and around the mineralized tubes (as in

Figure 1d), helping to preserve delicate structures from mechanical degradation (Grenne & Slack, 2003; Hein et al., 2008; Johannessen et al., 2020; Toner et al., 2012). Later, during diagenesis, the iron oxyhydroxides on the tubes and surrounding matrix would have matured to hematite and the amorphous silica to quartz, forming the studied jasper rock. This model is supported by experimental diagenesis of modern FeOB stalks at 170°C and 120 MPa, which transforms ferrihydrite to hematite and magnetite, and maintains morphologies at even higher temperatures (250°C) and pressures (140 MPa) (Picard et al., 2015), and also by the presence of hematitic filaments in modern Fe-oxide-Si mounds that precipitated from fluids at  $\geq 115^\circ\text{C}$  (Hein et al., 2008). Subsequent tectonic and regional metamorphic events would have caused multiple episode of quartz recrystallization and quartz veining in the jasper, leaving only small domains with preserved filaments, consistent with our observations.

Some (if not all) of the hematitic microfossils in the older, ca. 1.88 Ga Gunflint Iron Formation had ferrous iron-rich mineral intermediates such as greenalite, siderite, and pyrite (Lepot et al., 2017; Shapiro & Konhauser, 2015; Wacey et al., 2013). In this case, the ferrous intermediates could have formed from the diagenetic reduction

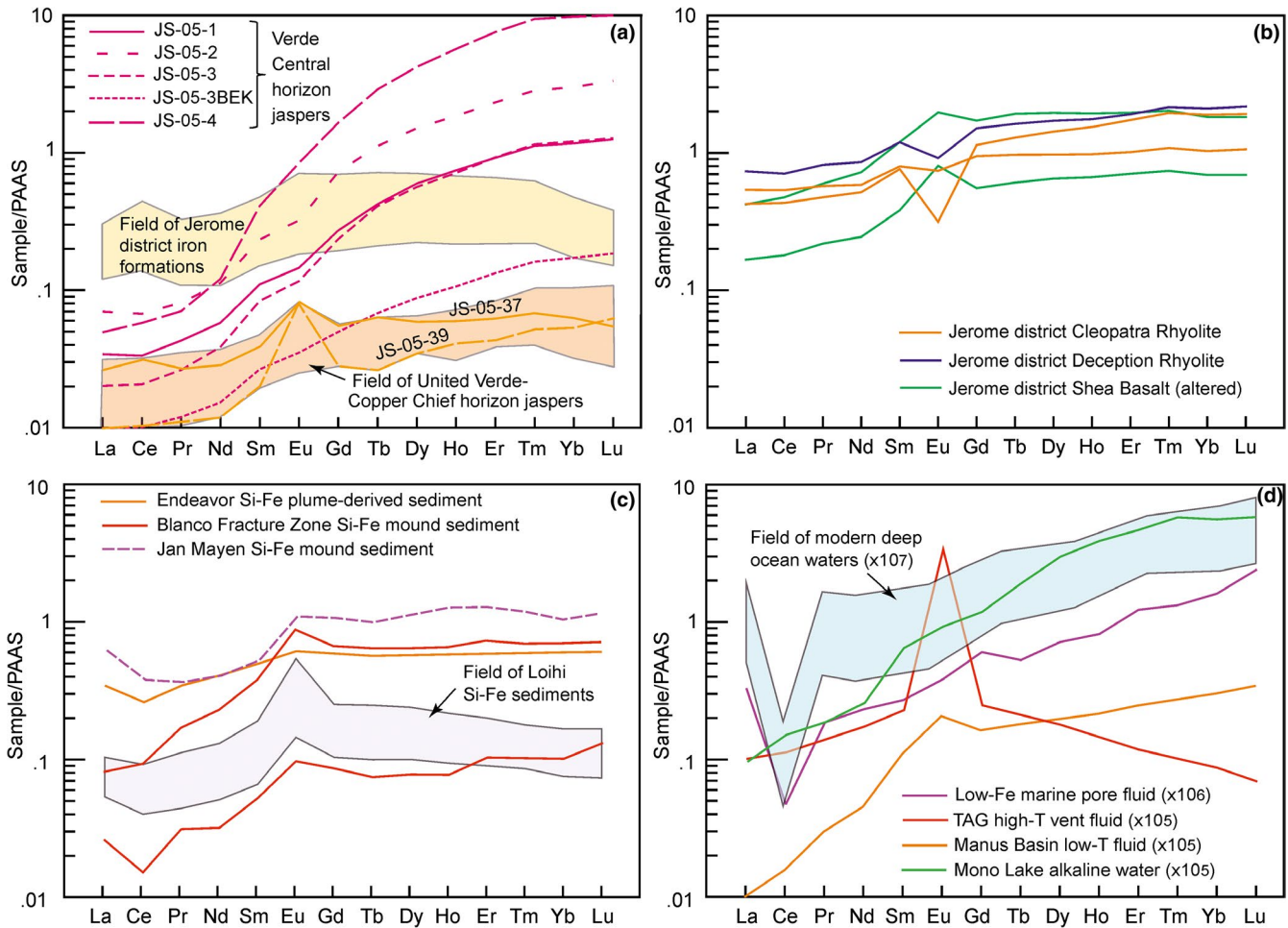


**FIGURE 8** Shale-normalized REE plots. (a) Paleoproterozoic jasper and iron formation from Verde mining district; note positive Eu anomalies for jasper samples JS-05-37 and JS-05-039. Data from Slack et al. (2007, Table S1; and Table 1). (b) Paleoproterozoic volcanic rocks from Verde district (see Figure 2b for stratigraphic positions); data from Slack et al. (2007, Table S1). (c) Modern Si-Fe seafloor-hydrothermal sediments; Endeavor data from Bao et al. (2008); Blanco Fracture Zone data from Hein et al. (2008); Loihi data from Edwards et al. (2011, Table S1); Jan Mayen data from Johannessen et al. (2017). (d) Modern waters; seawater data from Byrne and Sholkovitz (1996); Low-Fe marine pore fluid data from Haley et al. (2004); TAG data from Mills and Elderfield (1995); Manus Basin data from Douville et al. (1999); Mono Lake data from Johannesson and Lyons (1994). Shale normalization based on average Post-Archean Australian Shale (PAAS; Taylor & McLennan, 1985)

in ferric biominerals (Fadel et al., 2017; Lepot et al., 2017) before a late oxidation event returned them to their ferric state (Lepot et al., 2017; Shapiro & Konhauser, 2015). This mineralogical pathway is very unlikely for the VCJ filaments. Firstly, in contrast to the Gunflint Iron Formation studies, our detailed investigation of the VCJ filaments shows no clear indication of a ferrous mineral phase precursor. The Fe-Si-O mineral seen in one FIB section (Figure 7) may have formed by the weathering of such a ferrous mineral, or possibly the reduction in ferric biominerals, or even analytical beam damage. Moreover, the presence of rip-up clasts of jasper in tuffaceous sedimentary rocks in the sequence, where hematitic jasper clasts occur in a hematite-free tuff matrix (Figure 3c,d), demonstrates that formation of hematite (or a ferric oxyhydroxide precursor) occurred prior to diagenesis and greenschist-facies metamorphism, thus providing strong evidence against the oxidation within the enclosing tuffs by late oxidizing fluids. In addition, the likely transformation in the jasper precursor of

amorphous silica to chalcedony during early diagenesis (see Grenne & Slack, 2003) would make this highly siliceous rock more resistant to later oxidation than the more permeable lapilli tuff.

As well as the microaerobic FeOB, other modern micro-organisms use iron oxidation in their metabolic pathways, including freshwater microaerobic Betaproteobacteria, such as the stalk-forming *Gallionella* spp. and sheath-forming *Leptothrix* spp., acidophilic Actinobacteria and Archaea, phototrophic Alphabacteria, and bacteria belonging to a wide range of phylogenetic groups that are nitrate-dependent (e.g., Chan, Emerson, et al., 2016). However, in the marine realm, only a few of these produce filamentous structures that can be compared to the VCJ filaments and thus considered as potential alternative candidates for their origin. One of these microbes is the BS-1 strain of the purple, non-sulfur, alphaproteobacterium *Rhodomicoccus vannielii*, which is an anoxygenic photoferrotoph (e.g., Heising & Schink, 1998). This bacterium has oval cells ca. 2  $\mu\text{m}$  long and 1.5  $\mu\text{m}$

wide that link to others via filaments 0.3  $\mu\text{m}$  in diameter. The cells reproduce by budding along the filaments, which typically branch, leading to the formation of mesh-like colonies. Chi Fru et al. (2013) found fossilized examples of what could be this organism in early Quaternary banded jaspers that formed from hydrothermal vents in a restricted, shallow marine basin in Milos, Greece. The VCJ filaments share some of the features with the Milos structures, having elongated hematitic forms of roughly the same size, which have branches and form complex meshes. However, the VCJ filaments lack evidence of former cells occurring between linking filaments, hence are not the same as the Milos structures or colonies of *Rhodomicrobium vanielii*. Another more fundamental issue for comparing anoxygenic or oxygenic phototrophic micro-organisms with the VCJ filaments is that the latter formed in deep water, far below the photic zone. This constraint also precludes other explanations for the origin of the VCJ filaments, such as passive Fe-oxide precipitation in or on phototrophic organisms like cyanobacteria, as has been suggested for some of the microfossils (e.g., *Gunflintia*) in the Gunflint Iron Formation (Lepot et al., 2017; Shapiro & Konhauser, 2015).

Based on these morphological comparisons and paleoenvironmental arguments, we suggest that the VCJ filaments represent fossilized FeOB and that these FeOB could well have been microaerobic, living on the deep seafloor of an intraoceanic island arc in the mixing zone of Fe-rich, sulfide-poor, low-temperature, slightly acidic (see section 4.4) vent fluid and weakly oxygenated seawater. By their metabolic activity, these FeOB formed a percentage of the Fe precipitation that created the VCJ jasper units, together with abiogenic Fe precipitation from the vent fluid and distal fallout from a non-buoyant hydrothermal plume (see Slack et al., 2007).

Because of the morphological similarities between the VCJ filaments and FeOB from modern marine hydrothermal vent settings, it is tempting to suggest that the VCJ filaments were formed by Zetaproteobacteria and that they could thus act as a calibration point for molecular phylogenetic studies of micro-organisms (e.g., Betts et al., 2018). However, there are several reasons to be cautious in making this link. First, members of both marine Zetaproteobacteria and freshwater Betaproteobacteria produce very similar structures in iron-rich reducing habitats (compare twisted stalks of marine *Mariprofundus* and freshwater *Gallionella*, and non-branching sheaths of marine “veil-like mat” Zetaproteobacteria and freshwater *Leptothrix*; Fleming et al., 2013; Chan, Emerson, et al., 2016) and both Zetaproteobacteria and Betaproteobacteria occur in marine “iron mats” (Vander Roost et al., 2018). Second, there is likely to have been significant evolutionary changes in FeOB over the past 1.74 billion years, so the comparisons presented here between the VCJ filaments and modern FeOB point to analogues rather than phylogenetic proximity.

### 4.3 | Other potential Precambrian FeOB occurrences

In addition to the VCJ filaments, a number of other Precambrian occurrences of filamentous microstructures have been identified as

potential FeOB microfossils, all but one of which are from demonstrably shallow-water settings. These include the well-known hematitic microfossils belonging to the Paleoproterozoic Gunflint biota (see review in Javaux & Lepot, 2018). When these were first described from stromatolites in the Gunflint Iron Formation in Canada (Barghoorn & Tyler, 1965; Cloud, 1965), some of the microfossil morphologies were noted to be similar in size and shape to freshwater FeOB, such as the sheath-forming *Leptothrix* and the twisted, stalk-forming *Gallionella* (Barghoorn & Tyler, 1965; Cloud, 1965). In subsequent reports, authors tended to discount these earlier potential FeOB identifications and assign all Gunflint microfossils to various groups of cyanobacteria (e.g., Awramik & Barghoorn, 1977), an interpretation supported more recently by detailed studies of the typical Gunflint microfossils *Gunflintia* and *Huroniospora* by Shapiro and Konhauser (2015) and Lepot et al. (2017). However, based on iron isotope composition and REE patterns in the Gunflint and Biwabik Iron formations, Planavsky et al. (2009) resurrected the potential link between Gunflint Iron Formation microfossils and FeOB, although recent studies have shown that cyanobacteria can produce similar iron isotope fractionations (Mulholland et al., 2015).

Filamentous microstructures within intertidal to shallow subtidal ooidal and stromatolitic ironstones from the terminal Paleoproterozoic (ca. 1.65 to 1.64 Ga) Chuanlinggou Formation of North China have been interpreted as fossil FeOB by Lin et al. (2019). The filaments are spatially associated with silicified hematitic ooids and display a range of sizes (0.3–6.8  $\mu\text{m}$  in diameter and up to 100  $\mu\text{m}$  in length) and morphologies, including hematite-lined sheaths, some of which are twisted along their lengths. Unlike the VCJ filaments, the Chuanlinggou Formation microfossils do not branch and do form mat-like structures. Another shallow-water potential FeOB occurrence is in phosphatic stromatolites from the ca. 1.7 Ga Jhamarkotra Formation, India (Crosby et al. 2014). Here, microfossils are hosted by an apatite matrix and comprise bundles of subparallel filaments and filaments with radial growth patterns. The filaments are 100s of micrometers in length, and ca. 5 to 6  $\mu\text{m}$  in diameter with a central space (lumen) ca. 1 to 1.5  $\mu\text{m}$  in diameter, which locally show a twisted pattern. Some of the filaments display branching patterns and knobs. The filament walls are formed of a solid layer of goethite, and traces of kerogen occur in the lumens of some specimens. These Jhamarkotra Formation microfossils are quite convincing as being fossil FeOB. Fadel et al. (2017) interpreted three morphologies of carbonaceous microfossils associated with siderite and Fe-silicates as being potential iron-oxidizing bacteria from the ca. 2.45–2.43 Ga Turee Creek Group, Western Australia (Bekker et al., 2020). These microfossils come from a black chert nodule within the lower siliciclastic-dolostone member of the Kungarra Formation that contains four upward-shallowing depositional sequences with basal mudrocks overlain by fine-grained sandstones and dolostones deposited in a lower part of prodelta and off-shore to slope settings at the base and inner shelf to supratidal environments at the top (Barlow et al., 2016; Bekker et al., 2020). The microfossils display a filamentous morphology and are formed of variably preserved sheaths of kerogen, with lengths of 100s of micrometers

and diameters of 5 to 7.5  $\mu\text{m}$  (Type 2) and  $>3$   $\mu\text{m}$  (Type 3). The filaments have relatively constant diameters along their lengths and do not show any branching patterns. It is this character, together with the presence of kerogen, that distinguishes the Turee Creek Group microfossils from the VCJ filaments.

Hallberg and Broman (2018) reported microstructures from laminated carbonaceous shales in the Neoproterozoic (ca. 2.63 Ga) Jeerinah Formation, Australia, as representing fossil FeOB. The microstructures are lath-shaped with some twists, ca. 2 to 4  $\mu\text{m}$  across and up to 20  $\mu\text{m}$  long. They are formed of carbonaceous material and have low-Fe contents (max 8.1 wt%), so differ substantially in terms of mineralogy (and morphology) from the hematite-rich VCJ filaments, and indeed from other putative fossil FeOB. The oldest potential FeOB reported from the geological record are the microstructures in jaspers from the Eoarchean (minimum age 3.77 Ga, possibly 4.28 Ga) Nuvvuagittuq supracrustal belt (NSB), Canada (Dodd et al., 2017). These jaspers occur between sequences of variably altered tholeiitic and calc-alkaline metabasalt, locally with pillow lavas, and so formed at the same stage of volcanic evolution, most likely in a seafloor hydrothermal setting. The microstructures in the jaspers comprise filaments formed of hematite that are between 2 and 14  $\mu\text{m}$  in diameter and up to 500  $\mu\text{m}$  in length. Some of the filaments exhibit loose coils, some are branched, and some form twisted plates of hematite around a core that radiate from terminal knobs. Some of the hematite filaments occur within straight, quartz-filled cylindrical tubes 16 to 30  $\mu\text{m}$  in diameter and 80 to 400  $\mu\text{m}$  in length, with walls composed of dense, nanoscale hematite grains. Whereas some similarities exist between the VCJ and NSB filaments, there are also differences, including the lack of quartz-filled tubes in the VCJ samples and the fact that the NSB filaments do not form meshworks.

#### 4.4 | REE constraints on local fluid chemistry

The distinctive shale-normalized REE patterns of the VC jasper samples have extremely low LREE/HREE ratios in most cases (Figure 8a) and are very different from those typical of modern Fe-Si deposits (Figure 8c). In natural fluids, such very low LREE/HREE ratios are rare and are apparently limited to highly alkaline waters in restricted lakes such as Mono Lake in California (Johannesson & Lyons, 1994; Figure 8d) and Lake Van in Turkey (Möller & Bau, 1993). However, we consider it unlikely that the VC jaspers formed from such high-pH ( $>9$ ) fluids. Firstly, a model whereby the REE content of the jasper protoliths was controlled by alkaline ambient seawater can be ruled out based on the large variation in LREE/HREE ratios shown by the jaspers at this particular stratigraphic level. Second, a model involving precipitation from alkaline seafloor-hydrothermal fluids would require serpentinization of underlying ultramafic rocks within the hydrothermal convection system as occur in modern systems (e.g., Kelley et al., 2005; Palandri & Reed, 2004), but ultramafic rocks are absent in the Paleoproterozoic rhyolite to basalt sequence of the Verde district (Lindberg, 2008). Importantly, excluding such uncommon ultramafic settings, modern seafloor-hydrothermal fluids in

volcanic-dominated settings are characterized by low-pH values in the range of 2.0 to 5.8 (e.g., Hannington, 2014).

The REE patterns of some low-Fe marine pore fluids, excluding the large negative Ce anomaly, are broadly similar to those of the VC jaspers (Haley et al., 2004; Figure 8d). However, possible deposition of the VC jaspers from low-Fe fluids is rejected because these jaspers are relatively Fe-rich (Table 1), and assuming that the REEs precipitated with precursor iron oxyhydroxides as in modern analogues, the parent fluids would have had high, not low, iron contents. Development of the high HREE contents and very low LREE/HREE ratios by post-depositional alteration is also considered unlikely, because of the lack of supporting textural or mineralogical evidence for such alteration in either wall rocks or the jaspers and because of the typical low mobility of REEs during alteration of this type (Bau, 1991, 1993).

Our preferred model involves the deposition of primary silica iron oxyhydroxides from low-temperature and slightly acidic fluids. This model is linked to the experimental study of Liu et al. (2017) on differential sorption of REE to iron oxyhydroxides, which demonstrated that LREE versus HREE adsorption depends strongly on pH; a near-neutral to slightly alkaline fluid like normal seawater leads to little or no LREE/HREE fractionation, whereas a moderately acidic fluid with a pH of 5 to 6 will yield far lower LREE/HREE ratios in the precipitates. These data show that fluids spanning pH values of 0 to 3 units below that of normal modern seawater (pH = 7.8) can effectively produce a range of LREE/HREE ratios in iron oxyhydroxide similar to those observed for the VCJ samples, and also like the LREE/HREE range from VC jaspers to other Verde district jaspers as well as to modern Fe-Si precipitates (Figure 8a,c). Importantly, given the lack of definitive Ce anomalies in the VCJ samples, our REE data show very limited impact of redox processes on Ce and are thus inconsistent with precipitation of iron oxyhydroxides above the redoxcline via Fe oxidation. However, iron cannot be oxidized non-biologically below the redoxcline (e.g., Lewis & Landing, 1991), and our estimate of  $>500$  m for a minimum water depth puts this depositional site well below the photic zone. The only process known to oxidize iron below the photic zone and redoxcline is by microaerophilic bacteria, in agreement with our interpretations of a biological origin for the hematitic filaments in the VC jaspers.

The other jasper units in the Verde district, occurring at different stratigraphic levels, have very different REE patterns and greater lateral continuity (Figure 2b) and likely formed by plume fallout as suggested by Slack et al. (2007). This model is problematic for the VC jaspers, however, owing to the major dilution of hydrothermal fluids in plumes that occurs during venting and mixing with seawater. Such rapid mixing results instantly in a rise in pH to ambient seawater values within the plume (see Grenne & Slack, 2005), which conflicts with the variably low pH need to produce the distinctive REE patterns of the VC jaspers. The lack of positive Eu anomalies in these jasper samples (Figure 8a) also argues against formation from high-temperature fluids. Consequently, we propose that the jasper samples from the Verde Central horizon, and their contained microbial remains, formed not by plume fallout but from isolated,

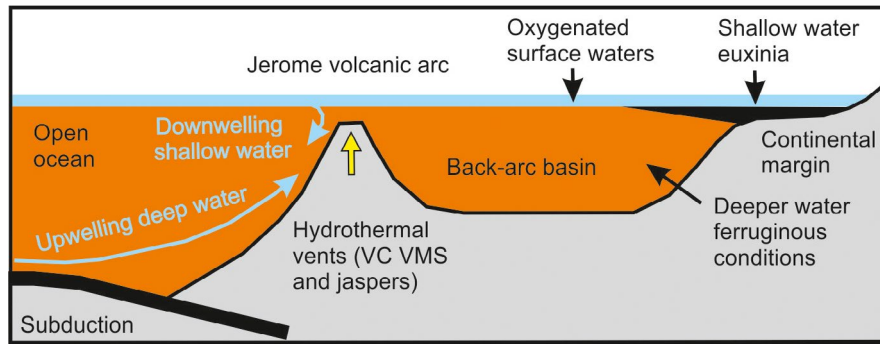


**FIGURE 9** Paleooceanographic redox model for the Jerome area volcanic arc. At some distance from the continental margin with associated ferruginous and euxinic conditions, we show the Jerome arc and associated hydrothermal activity being influenced by weakly oxygenated seawater, either downwelling from surface waters or upwelling from deeper waters driven by thermohaline circulation. The presence of the continental margin and back-arc basin is speculative. VC VMS, Verde Central volcanogenic massive sulfide

low-temperature hydrothermal vents that maintained relatively low, but variable, pH values during precipitation of iron oxyhydroxide phases. The hydrothermal fluids with low pH (5–6), indicated by very low LREE/HREE ratios in deposited iron oxyhydroxide phases (Liu et al., 2017), may have been involved in deposition of these phases within microbial mats having amorphous silica caps (see Sun et al., 2015; Zeng et al., 2012) that reduced dilution by ambient seawater. This interpretation is supported by low-pH values of 1.4 to 5.8 measured in some modern low-temperature hydrothermal systems, including within pore waters of actively forming iron oxyhydroxide deposits (Rouxel et al., 2018; Seewald et al., 2015). Such low-pH fluids likely formed in concert with a major component of magmatic fluid (Douville et al., 1999; Seewald et al., 2015).

#### 4.5 | Implications for Paleoproterozoic ocean redox and iron oxyhydroxide deposition

Our interpretation of the VCJ filaments as microaerobic FeOB (if correct) implies that some deep waters in the late Paleoproterozoic oceans were not anoxic, but rather weakly oxygenated, thus supporting the suboxic model of Slack et al. (2007). We speculate that the concentration of dissolved oxygen in the VCJ FeOB mats could have been between 3 and 30  $\mu\text{M}$ , with the lower limit from conditions for experimental growth of *Mariprofundus ferrooxydans* (Krepeski et al., 2013) and the upper limit from maximum  $\text{O}_2$  values measured within FeOB mats on Loihi Seamount (Glazer & Rouxel, 2009; Scott et al., 2017). This would imply equivalent, or perhaps even higher,  $\text{O}_2$  concentrations in the seawater overlying the mats. A minimum  $\text{O}_2$  concentration of 3  $\mu\text{M}$  for growth of FeOB mats is consistent with REE data for the modern Cariaco Basin, where a concentration spike in particulate iron (reflecting one or more  $\text{Fe}^{3+}$  phases) at the redox-cline, at 280 m water depth, coincides with water samples having ca. 2  $\mu\text{M}$   $\text{O}_2$  and 0  $\mu\text{M}$   $\text{H}_2\text{S}$  (De Baar et al., 1988). The lack of negative Ce anomalies and Mn-enrichment in the VMS-related Verde Central as well as other Verde district jaspers (Slack et al., 2007) is consistent with these suggested oxygen levels, including for the water sample

from 292 m depth in the Cariaco Basin that contains ca. 1  $\mu\text{M}$   $\text{O}_2$  and lacks a Ce anomaly ( $\text{Ce}/\text{Ce}^*_{\text{PAAS}} = 0.98$ ; calculated from data in De Baar et al., 1988). Formation of this redox state in deep 1.74 Ga seawater around the Jerome volcanic arc may have involved diffusion downwards of oxygenated surface waters, perhaps facilitated by the oceanographic situation analogous to modern seamounts, where both upwelling and downwelling can develop (e.g., Read & Pollard, 2017), and/or upwelling of variably oxygenated deep water driven by thermohaline circulation (Figure 9). The latter scenario is preferred here, based on patterns in the modern ocean where such oxygenated deep water transits the bases of major volcanic arcs in the South Pacific including the Kermadec Arc (e.g., Broecker, 2010).

We suggest that the Fe-Si protoliths of the VC jaspers formed at a minimum water depth of 500 m based on the Cu-rich nature of the ores, and a maximum depth of ~2,000 m based on the typically deepest examples of VMS-style hydrothermal activity known in modern volcanic arcs (Baker, 2017; de Ronde et al., 2003). This modern activity includes sites in the Kermadec Arc at Brothers and Giggenbach volcanoes, which contain Fe-Si deposits compositionally like the VC jaspers and in the latter area filamentous microbial remains (Jones et al., 2008; de Ronde et al., 2005).

Our proposal that weakly oxygenated deep waters existed around the Jerome volcanic arc is also consistent with anoxia (both euxinic and ferruginous conditions) occurring on contemporaneous continental margins, because such margins are where the greatest flux of nutrients via riverine run-off and upwelling would have existed, leading to increased primary productivity and thus oxygen depletion (Figure 9). It is important to emphasize that it is not known whether the mid-Proterozoic deep ocean was persistently and pervasively anoxic. Importantly, all existing geochemical proxies for extensive anoxia and euxinia in the mid-Proterozoic deep oceans do not require that redox state (e.g., Asael et al., 2018; Partin et al., 2013; Reinhard et al., 2013; Scott et al., 2008; Sheen et al., 2018). The deep ocean is not highly productive now and hence is not expected to have been highly productive in the mid-Proterozoic, and thus, it played an insignificant role in the burial of organic matter and consequently

redox-sensitive elements. Further, the paradigm of a persistently anoxic, ferruginous mid-Proterozoic deep ocean has shifted over the last decade to a consensus view that its redox state was variable over this long time interval (e.g., Diamond et al., 2018; Doyle et al., 2018; Planavsky et al., 2018; Shang et al., 2019; Sperling et al., 2014; Yang et al., 2017; Zhang et al., 2016, 2018). In our case, we cannot resolve whether our observations indicate episodic or pervasive weak oxygenation of the deep ocean, and hence, further studies of different windows of the mid-Proterozoic in separate basins are required. These deep ocean, weakly oxygenated waters once upwelled on the highly productive continental margins would rapidly lose their oxidation potential on mixing. We thus expect highly variable oxygen contents to have existed along shallow-to-deep transects across the mid-Proterozoic oceans (e.g., Planavsky et al., 2018).

Our finding of weakly oxygenated deep seawater in the late Paleoproterozoic may have implications for eukaryotic evolution, because at least during some time periods in the Proterozoic, oxygen was not confined to surface waters, and thus, a larger potentially habitable realm existed for these organisms, relative to that proposed in previous models (e.g., Martin et al., 2003). We further note that deep-water ( $\geq 500$  m) jasper and oxide-facies iron formation occur in other Proterozoic and Archean volcano-sedimentary sequences (Bekker et al., 2010; Slack et al., 2007, appendix 2), thus raising the possibility that some of these ancient seafloor-hydrothermal deposits also contain filamentous microfossils that, if identified and documented, could be used as proxies for the oxidation state of coeval deep seawater.

Our finding of FeOB within a Proterozoic iron-rich sediment is another piece of data supporting suggestions that biologically assisted Fe(II) oxidation was responsible for the deposition of BIF, at least to some extent (e.g., Chan, Emerson, et al., 2016; Holm, 1989; Konhauser et al., 2017; Posth et al., 2013). We emphasize that in the Verde Central case, deposition of the Fe-rich exhalites was closely associated with deep seafloor-hydrothermal activity, and hence, our results might not be applicable to shallow-water, Superior-type granular iron formation.

## ACKNOWLEDGMENTS

We are especially indebted to the late Paul Lindberg who provided guidance during fieldwork. CTSL thanks Simon Poulton for discussions about Proterozoic and Archaean paleoceanography. The Research Council of Norway is acknowledged for support to the NTNU NanoLab (Trondheim) through the Norwegian Micro- and Nano-Fabrication Facility, NorFab (197411/V30), and NORTEM infrastructure Grant 197405, TEM Gemini Centre, Norwegian University of Science and Technology (NTNU), Norway. TEM work was funded by the Bergen Research Foundation through a grant awarded to Nicola McLoughlin. Per Erik Vullum is thanked for invaluable assistance with the FIB-TEM analyses. Raman spectroscopy was funded through Swedish Research Council Contracts No. 2012-4364 and 2017-04129, and a Villum Investigator Grant to Don Canfield (No. 16518). We acknowledge the Paul Scherrer Institute, Villigen,

Switzerland, for provision of synchrotron radiation beamtime at the TOMCAT beamline X02DA of the SLS and thank Federica Marone for assistance. AB acknowledges support from NSERC Discovery and Accelerator programs and the University of Johannesburg in the form of a Distinguished Visiting Professorship. We thank three anonymous reviewers for comments and suggestions on an earlier version of the paper.

## DATA AVAILABILITY STATEMENT

The data that support the findings of this study are available in the Supplementary Material of this article.

## ORCID

Crispin T. S. Little  <https://orcid.org/0000-0002-1917-4460>  
 Karen C. Johannessen  <https://orcid.org/0000-0001-8790-8123>  
 Stefan Bengtson  <https://orcid.org/0000-0003-0206-5791>  
 Clara S. Chan  <https://orcid.org/0000-0003-1810-4994>  
 John F. Slack  <https://orcid.org/0000-0001-6600-3130>  
 Ingunn H. Thorseth  <https://orcid.org/0000-0003-3432-6968>  
 Tor Grenne  <https://orcid.org/0000-0003-1193-4127>  
 Olivier J. Rouxel  <https://orcid.org/0000-0002-1431-222X>  
 Andrey Bekker  <https://orcid.org/0000-0002-1154-0585>

## REFERENCES

- Anantharaman, K., Breier, J. A., & Dick, G. J. (2016). Metagenomic resolution of microbial functions in deep-sea hydrothermal plumes across the Eastern Lau Spreading Center. *ISME Journal*, 10, 225–239. <https://doi.org/10.1038/ismej.2015.81>
- Anderson, P. (1989). Proterozoic plate tectonic evolution of Arizona. *Arizona Geological Society Digest*, 17, 17–55.
- Asael, D., Rouxel, O., Poulton, S. W., Lyons, T. W., & Bekker, A. (2018). Molybdenum record from black shales indicates oscillating atmospheric oxygen levels in the early Paleoproterozoic. *American Journal of Science*, 318, 275–299. <https://doi.org/10.2475/03.2018.01>
- Awramik, S. M., & Barghoorn, E. S. (1977). The Gunflint microbiota. *Precambrian Research*, 5, 121–142. [https://doi.org/10.1016/0301-9268\(77\)90025-0](https://doi.org/10.1016/0301-9268(77)90025-0)
- Baker, E. T. (2017). Exploring the ocean for hydrothermal venting: New techniques, new discoveries, new insights. *Ore Geology Reviews*, 86, 55–69. <https://doi.org/10.1016/j.oregeorev.2017.02.006>
- Bao, S.-X., Zhou, H.-Y., Peng, X.-T., Ji, F.-W., & Yao, H.-Q. (2008). Geochemistry of REE and yttrium in hydrothermal fluids from the Endeavor segment, Juan de Fuca Ridge. *Geochemical Journal*, 42, 359–370.
- Barghoorn, E. S., & Tyler, S. A. (1965). Microorganisms from the Gunflint Chert. *Science*, 147, 563–577.
- Barlow, E., Van Kranendonk, M. J., Yamaguchi, K. E., Ikehara, M., & Lepland, A. (2016). Lithostratigraphic analysis of a new stromatolite-thrombolite reef from across the rise of atmospheric oxygen in the Paleoproterozoic Turee Creek Group, Western Australia. *Geobiology*, 14, 317–343. <https://doi.org/10.1111/gbi.12175>
- Bau, M. (1991). Rare-earth element mobility during hydrothermal and metamorphic fluid-rock interaction and the significance of the oxidation state of europium. *Chemical Geology*, 93, 219–230. [https://doi.org/10.1016/0009-2541\(91\)90115-8](https://doi.org/10.1016/0009-2541(91)90115-8)
- Bau, M. (1993). Effects of syn- and post-depositional processes on the rare-earth element distribution in Precambrian iron-formations. *European Journal of Mineralogy*, 5, 257–267. <https://doi.org/10.1127/ejm/5/2/0257>

- Beaulieu, S. E., Baker, E. T., German, C. R., & Maffei, A. (2013). An authoritative global database for active submarine hydrothermal vent fields. *Geochemistry Geophysics Geosystems*, 14, 4892–4905. <https://doi.org/10.1002/2013GC004998>
- Bekker, A., Holland, H. D., Wang, P. L., Rumble, D., Stein, H. J., Hannah, J. L., Coetzee, L. L., & Beukes, N. J. (2004). Dating the rise of atmospheric oxygen. *Nature*, 427, 117–120. <https://doi.org/10.1038/nature02260>
- Bekker, A., Krapež, B., & Karhu, J. A. (2020). Correlation of the stratigraphic cover of the Pilbara and Kaapvaal cratons recording the lead up to Paleoproterozoic Icehouse and the GOE. *Earth Science Reviews*, 211, 103389. <https://doi.org/10.1016/j.earscirev.2020.103389>
- Bekker, A., Slack, J. F., Planavsky, N., Krapež, B., Hofmann, A., Konhäuser, K. O., & Rouxel, O. J. (2010). Iron formation: The sedimentary product of a complex interplay among mantle, tectonic, oceanic, and biospheric processes. *Economic Geology*, 105, 467–508. <https://doi.org/10.2113/gsecongeo.105.3.467>
- Bennett, S. A., Toner, B. M., Barco, R., & Edwards, K. J. (2014). Carbon adsorption onto Fe oxyhydroxide stalks produced by a lithotrophic iron-oxidizing bacteria. *Geobiology*, 12, 146–156. <https://doi.org/10.1111/gbi.12074>
- Betts, H. C., Puttick, M. N., Clark, J. W., Williams, T. A., Donoghue, P. C., & Pisani, D. (2018). Integrated genomic and fossil evidence illuminates life's early evolution and eukaryote origin. *Nature Ecology and Evolution*, 2, 1556–1562. <https://doi.org/10.1038/s41559-018-0644-x>
- Briggs, D. F. (2018). *History of the Verde mining district, Jerome, Arizona*. Arizona Geological Survey Contributed Report CR-18-D, 85.
- Broecker, W. S. (2010). *The great ocean conveyor* (p. 176). Princeton University Press.
- Buick, R. (1990). Microfossil recognition in Archean rocks: An appraisal of spheroids and filaments from a 3500 m.y. old chert-barite unit at North Pole, Western Australia. *Palaio*, 5, 441–459. <https://doi.org/10.2307/3514837>
- Byrne, R. H., & Sholkovitz, E. R. (1996). Marine chemistry and geochemistry of the lanthanides. In K. A. Gschneidner, & L. Eyring (Eds.), *Handbook on the physics and chemistry of the rare earths* (pp. 497–593). Elsevier.
- Cady, S. L., Farmer, J. D., Grotzinger, J. P., Schopf, J. W., & Steele, A. (2003). Morphological biosignatures and the search for life on Mars. *Astrobiology*, 3, 351–368. <https://doi.org/10.1089/153110703769016442>
- Canfield, D. E. (1998). A new model for Proterozoic ocean chemistry. *Nature*, 396, 450–453. <https://doi.org/10.1038/24839>
- Canfield, D. E. (2005). The early history of atmospheric oxygen: Homage to Robert M. Garrels. *Annual Review of Earth and Planetary Sciences*, 33, 1–36. <https://doi.org/10.1146/annurev.earth.33.092203.122711>
- Canfield, D. E., Poulton, S. W., Knoll, A. H., Narbonne, G. M., Ross, G., Goldberg, T., & Strauss, H. (2008). Ferruginous conditions dominated later Neoproterozoic deep-water chemistry. *Science*, 321, 949–952. <https://doi.org/10.1126/science.1154499>
- Chan, C. S., Emerson, D., & Luther, G. W. (2016). The role of microaerophilic Fe-oxidizing micro-organisms in producing banded iron formations. *Geobiology*, 14, 509–528. <https://doi.org/10.1111/gbi.12192>
- Chan, C. S., Fakra, S. C., Emerson, D., Fleming, E. J., & Edwards, K. J. (2011). Lithotrophic iron-oxidizing bacteria produce organic stalks to control mineral growth: Implications for biosignature formation. *The ISME Journal*, 5, 717–727. <https://doi.org/10.1038/ismej.2010.173>
- Chan, C. S., McAllister, S. M., Leavitt, A. H., Glazer, B. T., Krepski, S. T., & Emerson, D. (2016). The architecture of iron microbial mats reflects the adaptation of chemolithotrophic iron oxidation in freshwater and marine environments. *Frontiers in Microbiology*, 7, 1–18. <https://doi.org/10.3389/fmicb.2016.00796>
- Chi Fru, E., Ivarsson, M., Kiliyas, S. P., Bengtson, S., Belivanova, V., Marone, F., Fortin, D., Broman, C., & Stampanoni, M. (2013). Fossilized iron bacteria reveal a pathway to the biological origin of banded iron formations. *Nature Communications*, 4, 1–7.
- Chiu, B. K., Kato, S., McAllister, S. M., Field, E. K., & Chan, C. S. (2017). Novel pelagic iron-oxidizing Zetaproteobacteria from the Chesapeake Bay oxic-anoxic transition zone. *Frontiers in Microbiology*, 8, 1280. <https://doi.org/10.3389/fmicb.2017.01280>
- Cloud, P. (1965). The significance of the Gunflint (Precambrian) microflora. *Science*, 148, 27–35.
- Corliss, J. B., Dymond, J., Gordon, L. I., Edmond, J. M., von Herzen, R. P., Ballard, R. D., Green, K., Williams, D., Bainbridge, A., Crane, K., & van Andel, T. H. (1979). Submarine thermal springs on the Galápagos Rift. *Science*, 203, 1073–1083. <https://doi.org/10.1126/science.203.4385.1073>
- Crosby, C. H., Bailey, J. V., & Sharma, M. (2014). Fossil evidence of iron-oxidizing chemolithotrophy linked to phosphogenesis in the wake of the Great Oxidation Event. *Geology*, 42, 1015–1018. <https://doi.org/10.1130/G35922.1>
- Davis, R. E., & Moyer, C. L. (2008). Extreme spatial and temporal variability of hydrothermal microbial mat communities along the Mariana island arc and southern Mariana back-arc system. *Journal of Geophysical Research*, 113, B08S15. <https://doi.org/10.1029/2007JB005413>
- Davis, R. E., Stakes, D. S., Wheat, C. G., & Moyer, C. L. (2009). Bacterial variability within an iron-silica-manganese-rich hydrothermal mound located off-axis at the Cleft segment, Juan de Fuca Ridge. *Geomicrobiology Journal*, 26, 570–580. <https://doi.org/10.1080/01490450902889080>
- De Baar, H. J. W., German, C. R., Elderfield, H., & van Gaans, P. (1988). Rare earth element distribution in anoxic waters of the Cariaco Trench. *Geochimica Et Cosmochimica Acta*, 52, 1203–1219.
- de Ronde, C. E. J., Hannington, M. D., Stoffers, P., Wright, I. C., Ditchburn, R. G., Reyes, A. G., Baker, E. T., Massoth, G. J., Lupton, J. E., Walker, S. L., Greene, R. R., Soong, C. W. R., Ishibashi, J., Lebon, G. T., Bray, C. J., & Resing, J. A. (2005). Evolution of a submarine magmatic-hydrothermal system: Brothers Volcano, southern Kermadec Arc, New Zealand. *Economic Geology*, 100, 1097–1133. <https://doi.org/10.2113/gsecongeo.100.6.1097>
- De Ronde, C. E. J., Massoth, G. J., Baker, E. T., & Lupton, J. E. (2003). Submarine hydrothermal venting related to volcanic arcs. In S. F. Simmons, & I. Graham (Eds.), *Volcanic, geothermal, and ore-forming fluids: Rulers and witnesses of processes within the Earth* (pp. 91–110). Society of Economic Geologists Inc, Special Publication 10.
- Dekov, V. M., Lalonde, S. V., Kamenov, G. D., Bayon, G., Shanks, W. C. III, Fortin, D., Fouquet, Y., & Moscati, R. J. (2015). Geochemistry and mineralogy of a silica chimney from an inactive seafloor hydrothermal field (East Pacific Rise, 18°S). *Chemical Geology*, 415, 126–140. <https://doi.org/10.1016/j.chemgeo.2015.09.017>
- Diamond, C. W., Planavsky, N. J., Wang, C., & Lyons, T. W. (2018). What the ~1.4 Ga Xiamaling Formation can and cannot tell us about the mid-Proterozoic ocean. *Geobiology*, 16, 219–236.
- Dodd, M. S., Papineau, D., Grenne, T., Slack, J. F., Rittner, M., Pirajno, F., O'Neil, J., & Little, C. T. S. (2017). Evidence for early life in Earth's oldest hydrothermal vent precipitates. *Nature*, 543, 60–65. <https://doi.org/10.1038/nature21377>
- Douville, E., Bienvenu, P., Charlou, J. L., Donval, J. P., Fouquet, Y., Appriou, P., & Gamo, T. (1999). Yttrium and rare earth elements in fluids from various deep-sea hydrothermal systems. *Geochimica Et Cosmochimica Acta*, 63, 627–643. [https://doi.org/10.1016/S0016-7037\(99\)00024-1](https://doi.org/10.1016/S0016-7037(99)00024-1)
- Doyle, K. A., Poulton, S. W., Newton, R. J., Podkovyrov, V. N., & Bekker, A. (2018). Shallow water anoxia in the Mesoproterozoic ocean: Evidence from the Bashkir Meganticlinorium, Southern Urals. *Precambrian Research*, 317, 196–210. <https://doi.org/10.1016/j.precamres.2018.09.001>

- Duhig, N. C., Davidson, G. J., & Stolz, J. (1992). Microbial involvement in the formation of Cambrian sea-floor silica-iron oxide deposits, Australia. *Geology*, 20, 511–514. [https://doi.org/10.1130/0091-7613\(1992\)020<0511:MIITFO>2.3.CO;2](https://doi.org/10.1130/0091-7613(1992)020<0511:MIITFO>2.3.CO;2)
- Edwards, K. J., Glazer, B. T., Rouxel, O. J., Bach, W., Emerson, D., Davis, R. E., Toner, B. M., Chan, C. S., Tebo, B. M., Staudigel, H., & Moyer, C. L. (2011). Ultra-diffuse hydrothermal venting supports Fe-oxidizing bacteria and massive uranium deposition at 5000m off Hawaii. *The ISME Journal*, 5, 1748–1758.
- Emerson, D. (2009). Potential for iron-reduction and iron-cycling in iron oxyhydroxide-rich microbial mats at Loihi Seamount. *Geomicrobiology Journal*, 26, 639–647. <https://doi.org/10.1080/01490450903269985>
- Emerson, D., & Moyer, C. L. (2002). Neutrophilic Fe-oxidizing bacteria are abundant at the Loihi Seamount hydrothermal vents and play a major role in Fe oxide deposition. *Applied and Environmental Microbiology*, 68, 3085–3093. <https://doi.org/10.1128/AEM.68.6.3085-3093.2002>
- Emerson, D., Rentz, J. A., Lilburn, T. G., Davis, R. E., Aldrich, H., Chan, C., & Moyer, C. L. (2007). A novel lineage of Proteobacteria involved in formation of marine Fe-oxidizing microbial mat communities. *PLoS One*, 2(8), e667. <https://doi.org/10.1371/journal.pone.0000667>
- Emerson, D., & Revsbech, N. P. (1994). Investigation of an iron-oxidizing microbial mat community located near Aarhus, Denmark: Field studies. *Applied and Environmental Microbiology*, 60, 4022–4031. <https://doi.org/10.1128/AEM.60.11.4022-4031.1994>
- Emerson, D., Scott, J. J., Leavitt, A., Fleming, E., & Moyer, C. (2017). In situ estimates of iron-oxidation and accretion rates for iron-oxidizing bacterial mats at Lō'ihi Seamount. *Deep-Sea Research (I)*, 126, 31–39. <https://doi.org/10.1016/j.dsr.2017.05.011>
- Fadel, A., Lepot, K., Busigny, V., Addad, A., & Troadec, D. (2017). Iron mineralization and taphonomy of microfossils of the 2.45–2.21 Ga Turee Creek Group, Western Australia. *Precambrian Research*, 298, 530–551. <https://doi.org/10.1016/j.precamres.2017.07.003>
- Fleming, E. J., Davis, R., McAllister, S., Chan, C. S., Moyer, C. L., Tebo, B., & Emerson, D. (2013). Hidden in plain sight: Discovery of sheath forming, Fe-oxidizing Zetaproteobacteria at Loihi Seamount. *FEMS Microbial Ecology*, 85, 116–127.
- Forget, N., Murdock, S., & Juniper, S. (2010). Bacterial diversity in Fe-rich hydrothermal sediments at two south Tonga Arc submarine volcanoes. *Geobiology*, 8, 417–432. <https://doi.org/10.1111/j.1472-4669.2010.00247.x>
- Fouquet, Y., Cambon, P., Etoubleau, J., Charlou, J. L., Ondreas, H., Barriga, F. J. A. S., Cherkashov, G., Semkova, T., Poroshina, I., Bohn, M., Donval, J. P., Henry, K., Murphy, P., & Rouxel, O. (2010). Geodiversity of hydrothermal processes along the Mid-Atlantic Ridge and ultramafic-hosted mineralization: A new type of oceanic Cu-Zn-Co-Au volcanogenic massive sulfide deposit. In P. Rona (Ed.), *Diversity of hydrothermal systems on slow-spreading ocean ridges* (pp. 321–367). American Geophysical Union. Geophysical Monograph 188.
- Garcia-Ruiz, J. M., Melero-García, E., & Hyde, S. T. (2009). Morphogenesis of self-assembled nanocrystalline materials of barium carbonate and silica. *Science*, 323, 362–365. <https://doi.org/10.1126/science.1165349>
- Glazer, B. T., & Rouxel, O. J. (2009). Redox speciation and distribution within diverse iron-dominated microbial habitats at Loihi Seamount. *Geomicrobiology Journal*, 26, 606–622. <https://doi.org/10.1080/01490450903263392>
- Grenne, T., & Slack, J. F. (2003). Bedded jaspers of the Ordovician Løkken ophiolite, Norway: Seafloor deposition and diagenetic maturation of hydrothermal plume-derived silica-iron gels. *Mineralium Deposita*, 38, 625–639. <https://doi.org/10.1007/s00126-003-0346-3>
- Grenne, T., & Slack, J. F. (2005). Geochemistry of jasper beds from the Ordovician Løkken ophiolite, Norway: Origin of proximal and distal siliceous exhalites. *Economic Geology*, 100, 1511–1527.
- Gustin, M. S. (1990). Stratigraphy and alteration of the host rocks, United Verde massive sulfide deposit, Jerome, Arizona. *Economic Geology*, 85, 29–49. <https://doi.org/10.2113/gsecongeo.85.1.29>
- Haley, B. A., Klinkhammer, G. P., & McManus, J. (2004). Rare earth elements in pore waters of marine sediments. *Geochimica Et Cosmochimica Acta*, 68, 1265–1279. <https://doi.org/10.1016/j.gca.2003.09.012>
- Hallberg, R. O., & Broman, C. (2018). Microbial fossils in the 2.63 Ga Jeerinah Formation, Western Australia—Evidence of microbial oxidation. *Geomicrobiology Journal*, 35, 255–260. <https://doi.org/10.1080/01490451.2017.1348407>
- Hannington, M. D. (2014). Volcanogenic massive sulfide deposits. In S. D. Scott (Ed.), *Geochemistry of mineral deposits. Treatise on geochemistry* (2nd ed., vol. 13, pp. 463–488). Elsevier.
- Hannington, M. D., Jonasson, I. R., Hertz, P. M., & Petersen, S. (1995). Physical and chemical processes of seafloor mineralization at mid-ocean ridges. In S. E. Humphris, R. A. Zierenberg, L. S. Mullineaux, & R. E. Thomson (Eds.), *Seafloor hydrothermal systems: Physical, chemical, biological, and geological interactions* (pp. 115–157). American Geophysical Union. Geophysical Monograph 91.
- Hein, J. R., Clague, D. A., Koski, R. A., Embley, R. W., & Dunham, R. E. (2008). Metalliferous sediment and a silica-hematite deposit within the Blanco Fracture Zone, northeast Pacific. *Marine Georesources & Geotechnology*, 26, 317–339. <https://doi.org/10.1080/10641190802430986>
- Heising, S., & Schink, B. (1998). Phototrophic oxidation of ferrous iron by a *Rhodomicoccus vannielii* strain. *Microbiology*, 144, 2263–2269. <https://doi.org/10.1099/00221287-144-8-2263>
- Holm, N. G. (1989). The <sup>13</sup>C/<sup>12</sup>C ratios of siderite and organic matter of a modern metalliferous hydrothermal sediment and their implications for banded iron formations. *Chemical Geology*, 77, 41–45. [https://doi.org/10.1016/0009-2541\(89\)90013-2](https://doi.org/10.1016/0009-2541(89)90013-2)
- Hopkinson, L., Roberts, S., Herrington, R., & Wilkinson, J. (1998). Self-organization of submarine hydrothermal siliceous deposits: Evidence from the TAG hydrothermal mound, 26°N Mid-Atlantic Ridge. *Geology*, 26, 347–350. [https://doi.org/10.1130/0091-7613\(1998\)026<0347:SOOSHS>2.3.CO;2](https://doi.org/10.1130/0091-7613(1998)026<0347:SOOSHS>2.3.CO;2)
- Huston, D. L., Pehrrson, S., Eglington, B. M., & Zaw, K. (2010). The geology and metallogeny of volcanic-hosted massive sulphide deposits: Variations through geologic time and with tectonic setting. *Economic Geology*, 105, 571–591.
- Javaux, E. J., & Lepot, K. (2018). The Paleoproterozoic fossil record: Implications for the evolution of the biosphere during Earth's middle-age. *Earth-Science Reviews*, 176, 68–86. <https://doi.org/10.1016/j.earscirev.2017.10.001>
- Johannessen, K. C., McLoughlin, N., Vullum, P. E., & Thorseth, I. (2020). On the biogenicity of Fe-oxyhydroxide filaments in silicified low-temperature hydrothermal deposits: Implications for the identification of Fe-oxidizing bacteria in the rock record. *Geobiology*, 18, 31–53. <https://doi.org/10.1111/gbi.12363>
- Johannessen, K. C., Vander Roost, J., Dahle, H., Dundas, S. H., Pedersen, R. B., & Thorseth, I. H. (2017). Environmental controls on biomineralization and Fe-mound formation in a low-temperature hydrothermal system at the Jan Mayen vent fields. *Geochimica Et Cosmochimica Acta*, 202, 101–123. <https://doi.org/10.1016/j.gca.2016.12.016>
- Johannesson, K. H., & Lyons, W. B. (1994). The rare earth element geochemistry of Mono Lake water and the importance of carbonate complexing. *Limnology and Oceanography*, 39, 1141–1154. <https://doi.org/10.4319/lo.1994.39.5.1141>
- Jones, B., de Ronde, C. E. J., & Renaut, R. W. (2008). Mineralized microbes from Giggenbach submarine volcano. *Journal of Geophysical Research*, 113(B8, 13). <https://doi.org/10.1029/2007JB005482>
- Juniper, S. K., & Fouquet, Y. (1988). Filamentous iron silica deposits from modern and ancient hydrothermal sites. *Canadian Mineralogist*, 26, 859–869.

- Kamber, B. S., Webb, G. E., & Gallagher, M. (2014). The rare earth element signal in Archaean microbial carbonate: Information on ocean redox and biogenicity. *Journal of the Geological Society of London*, *171*, 745–763. <https://doi.org/10.1144/jgs2013-110>
- Karl, D. M., McMurtry, G. M., Malahoff, A., & Garcia, M. O. (1988). Loihi Seamount, Hawaii: A mid-plate volcano with a distinctive hydrothermal system. *Nature*, *335*, 532–535. <https://doi.org/10.1038/335532a0>
- Kelley, D. S., Karson, J. A., Früh-Green, G. L., Yoerger, D. R., Shank, T. M., Butterfield, D. A., Hayes, J. M., Schrenk, M. O., Olson, E. J., Proskurowski, G., & Jakuba, M. (2005). A serpentinite-hosted ecosystem: The Lost City hydrothermal field. *Science*, *307*, 1428–1434. <https://doi.org/10.1126/science.1102556>
- Kendall, B., Creaser, R. A., Gordon, G. W., & Anbar, A. D. (2009). Re-Os and Mo isotope systematics of black shales from the Middle Proterozoic Velkerri and Wollogorang formations, McArthur basin, northern Australia. *Geochimica Et Cosmochimica Acta*, *73*, 2534–2558. <https://doi.org/10.1016/j.gca.2009.02.013>
- Konhauser, K. O., Planavsky, N. J., Hardisty, D. S., Robbins, L. J., Warchola, T. J., Haugaard, R., Lalonde, S. V., Partin, C. A., Oonk, P. B. H., Tsikos, H., Lyons, T. W., Bekker, A., & Johnson, C. M. (2017). Iron formations: A global record of Neoproterozoic to Palaeoproterozoic environmental history. *Earth-Science Reviews*, *172*, 140–177. <https://doi.org/10.1016/j.earscirev.2017.06.012>
- Krepeski, S. T., Emerson, D., Hredzak-Showalter, P. L., Luther, G. W. III, & Chan, C. S. (2013). Morphology of biogenic iron oxides records microbial physiology and environmental conditions: Toward interpreting iron microfossils. *Geobiology*, *11*, 457–471. <https://doi.org/10.1111/gbi.12043>
- Langley, S., Igric, P., Takahashi, Y., Sakai, Y., Fortin, D., Hannington, M. D., & Schwarz-Schampera, U. (2009). Preliminary characterization and biological reduction of putative biogenic iron oxides (BIOS) from the Tonga-Kermadec Arc, southwest Pacific Ocean. *Geobiology*, *7*, 35–49. <https://doi.org/10.1111/j.1472-4669.2008.00180.x>
- Laufer, K., Nordhoff, M., Halama, M., Martinez, R. E., Obst, M., Nowak, M., Stryhanyuk, H., Richnow, H. H., & Kappler, A. (2017). Microaerophilic Fe(II)-oxidizing Zetaproteobacteria isolated from low-Fe marine coastal sediments: Physiology and composition of their twisted stalks. *Applied and Environmental Microbiology*, *83*, 1–20. <https://doi.org/10.1128/AEM.03118-16>
- Lawrence, M. G., & Kamber, B. S. (2006). The behaviour of the rare earth elements during estuarine mixing—Revisited. *Marine Chemistry*, *100*, 147–161. <https://doi.org/10.1016/j.marchem.2005.11.007>
- Lepot, K., Addad, A., Knoll, A. H., Wang, J., Troadec, D., Béch e, A., & Javaux, E. J. (2017). Iron minerals within specific microfossil morphospecies of the 1.88 Ga Gunflint Formation. *Nature Communications*, *8*(1), 1–11. <https://doi.org/10.1038/ncomms14890>
- Lewis, B. L., & Landing, W. M. (1991). The biogeochemistry of manganese and iron in the Black Sea. *Deep-Sea Research*, *38*(Suppl. 2), S773–S803. [https://doi.org/10.1016/S0198-0149\(10\)80009-3](https://doi.org/10.1016/S0198-0149(10)80009-3)
- Li, J., Zhou, H., Peng, X., Wu, Z., Chen, S., & Fang, J. (2012). Microbial diversity and biomineralization in low-temperature hydrothermal iron-silica-rich precipitates of the Lau Basin hydrothermal field. *FEMS Microbiology Ecology*, *81*, 205–216. <https://doi.org/10.1111/j.1574-6941.2012.01367.x>
- Lin, Y., Tang, D., Shi, X., Zhou, X., & Huang, K. (2019). Shallow-marine ironstones formed by microaerophilic iron-oxidizing bacteria in terminal Paleoproterozoic. *Gondwana Research*, *76*, 1–18. <https://doi.org/10.1016/j.gr.2019.06.004>
- Lindberg, P. A. (2008). Early Proterozoic volcanogenic massive sulfide ore deposits, Jerome, Arizona, USA. *Arizona Geological Society Digest*, *22*, 601–610.
- Little, C. T. S., Glynn, S. E. J., & Mills, R. A. (2004). Four-hundred-and-ninety-million-year record of bacteriogenic iron oxide precipitation at sea-floor hydrothermal vents. *Geomicrobiology Journal*, *21*, 415–429. <https://doi.org/10.1080/01490450490485845>
- Liu, H., Pourret, O., Guo, H., & Bonhoure, J. (2017). Rare earth elements sorption to iron oxyhydroxide: Model development and application to groundwater. *Applied Geochemistry*, *87*, 158–166. <https://doi.org/10.1016/j.apgeochem.2017.10.020>
- Marone, F., & Stampanoni, M. (2012). Regridding reconstruction algorithm for real-time tomographic imaging. *Journal of Synchrotron Radiation*, *19*, 1029–1037. <https://doi.org/10.1107/S0909049512032864>
- Martin, W., Rotte, C., Hoffmeister, M., Theissen, U., Gelius-Dietrich, G., Ahr, S., & Henze, K. (2003). Early cell evolution, eukaryotes, anoxygenic sulfide, oxygen, fungi first (?), and a tree of genomes revisited. *IUBMB Life*, *55*, 193–204. <https://doi.org/10.1080/1521654031000141231>
- McAllister, S. M., Moore, R. M., Gartman, A., Luther, G. W. III, Emerson, D., & Chan, C. S. (2019). The Fe(II)-oxidizing Zetaproteobacteria: Historical, ecological and genomic perspectives. *FEMS Microbiology Ecology*, *95*, 1–18.
- McAllister, S. M., Polson, S. W., Butterfield, D. A., Glazer, B. T., Sylvan, J. B., & Chan, C. S. (2020). Validating the Cyc2 neutrophilic iron oxidation pathway using meta-omics of zetaproteobacteria iron mats at marine hydrothermal vents. *mSystems*, *5*, e00553-19.
- McMahon, S. (2019). Earth's earliest and deepest purported fossils may be iron-mineralized chemical gardens. *Proceedings of the Royal Society B*, *286*, 20192410. <https://doi.org/10.1098/rspb.2019.2410>
- Meyer, K. M., & Kump, L. R. (2008). Oceanic euxinia in Earth history: Causes and consequences. *Annual Review of Earth and Planetary Sciences*, *36*, 251–288. <https://doi.org/10.1146/annurev-earth.36.031207.124256>
- Mills, R. A., & Elderfield, H. (1995). Rare earth element geochemistry of hydrothermal deposits from the active TAG Mound, 26°N Mid-Atlantic Ridge. *Geochimica Et Cosmochimica Acta*, *59*, 3511–3524. [https://doi.org/10.1016/0016-7037\(95\)00224-N](https://doi.org/10.1016/0016-7037(95)00224-N)
- Möller, P., & Bau, M. (1993). Rare-earth patterns with positive cerium anomaly in alkaline waters from Lake Van, Turkey. *Earth and Planetary Science Letters*, *117*, 671–676. [https://doi.org/10.1016/0012-821X\(93\)90110-U](https://doi.org/10.1016/0012-821X(93)90110-U)
- Mulholland, D. S., Poitrasson, F., Shirokova, L. S., González, A. G., Pokrovsky, O. S., Boaventura, G. R., & Vieira, L. C. (2015). Iron isotope fractionation during Fe (II) and Fe (III) adsorption on cyanobacteria. *Chemical Geology*, *400*, 24–33. <https://doi.org/10.1016/j.chemgeo.2015.01.017>
- Ohmoto, H., Watanabe, Y., Ikemi, H., Poulson, S. R., & Taylor, B. E. (2006). Sulphur isotope evidence for an oxic Archaean atmosphere. *Nature*, *442*, 909–911. <https://doi.org/10.1038/nature05044>
- Palandri, J. L., & Reed, M. H. (2004). Geochemical models of metasomatism in ultramafic systems: Serpentinization, rodingitization, and sea floor carbonate chimney precipitation. *Geochimica Et Cosmochimica Acta*, *68*, 1115–1133. <https://doi.org/10.1016/j.gca.2003.08.006>
- Partin, C. A., Bekker, A., Planavsky, N. J., Scott, C. T., Gill, B. G., Li, C., Podkovyrov, V., Maslov, A., Konhauser, K. O., Lalonde, S. V., Love, G. D., Poulton, S. W., & Lyons, T. W. (2013). Large-scale fluctuations in Precambrian atmospheric and oceanic oxygen levels from the record of U in shales. *Earth and Planetary Science Letters*, *369–370*, 284–293. <https://doi.org/10.1016/j.epsl.2013.03.031>
- Pedersen, R. B., Thorseth, I. H., Nygaard, T. E., Lilley, M. D., & Kelley, D. S. (2010). Hydrothermal activity at the Arctic mid-ocean ridges. In P. A. Rona, C. W. Devey, J. Dymant, & B. J. Murton (Eds.), *Diversity of hydrothermal systems on slow spreading ocean ridges* (pp. 67–89). American Geophysical Union. Geophysical Monograph 188.
- Peng, X., Ta, K., Chen, S., Zhang, L., & Xu, H. (2015). Coexistence of Fe(II)- and Mn(II)-oxidizing bacteria govern the formation of deep sea uranium deposits. *Geochimica Et Cosmochimica Acta*, *169*, 200–216. <https://doi.org/10.1016/j.gca.2015.09.011>
- Petersen, S., Hannington, M. D., Hölz, S., Krättschell, A., Klischies, M., Graber, S., Anderson, M. O., Jamieson, J. W., Grant, H. L. J., & Murton, B.

- J. (2019). *Same, same, but different: Recent advances in our understanding of modern seafloor hydrothermal systems*. Glasgow, Scotland, University of Glasgow, Proceedings of the 15th Biennial SGA Meeting, 1, 80–82.
- Picard, A., Kappler, A., Schmid, G., Quaroni, L., & Obst, M. (2015). Experimental diagenesis of organo-mineral structures formed by microaerophilic Fe(II)-oxidizing bacteria. *Nature Communications*, 6, 6277. <https://doi.org/10.1038/ncomms7277>
- Planavsky, N. J., McGoldrick, P., Scott, C. T., Li, C., Reinhard, C. T., Kelly, A. E., Chu, X., Bekker, A., Love, G. D., & Lyons, T. W. (2011). Widespread iron-rich conditions in the mid-Proterozoic ocean. *Nature*, 477, 448–452. <https://doi.org/10.1038/nature10327>
- Planavsky, N., Rouxel, O., Bekker, A., Shapiro, R., Fralick, P., & Knudsen, A. (2009). Iron-oxidizing microbial ecosystems thrived in late Paleoproterozoic redox-stratified oceans. *Earth and Planetary Science Letters*, 286, 230–242. <https://doi.org/10.1016/j.epsl.2009.06.033>
- Planavsky, N. J., Slack, J. F., Cannon, W. F., O'Connell, B., Isson, T. T., Asael, D., Jackson, J. C., Hardisty, D. S., Lyons, T. W., & Bekker, A. (2018). Evidence for episodic oxygenation in a weakly redox-buffered deep mid-Proterozoic ocean. *Chemical Geology*, 483, 581–594. <https://doi.org/10.1016/j.chemgeo.2018.03.028>
- Posth, N. R., Konhauser, K. O., & Kappler, A. (2013). Microbiological processes in banded iron formation deposition. *Sedimentology*, 60, 1733–1754. <https://doi.org/10.1111/sed.12051>
- Poulton, S. W., & Canfield, D. E. (2011). Ferruginous conditions: A dominant feature of the ocean through Earth's history. *Elements*, 7, 107–112. <https://doi.org/10.2113/gselements.7.2.107>
- Poulton, S. W., Fralick, P. W., & Canfield, D. E. (2004). The transition to a sulphidic ocean ~1.84 billion years ago. *Nature*, 431, 173–177.
- Poulton, S. W., Fralick, P. W., & Canfield, D. E. (2010). Spatial variability in oceanic redox structure 1.8 billion years ago. *Nature Geoscience*, 3, 486–490.
- Read, R., & Pollard, R. (2017). An introduction to the physical oceanography of six seamounts in the southwest Indian Ocean. *Deep Sea Research (II)*, 136, 44–58. <https://doi.org/10.1016/j.dsr2.2015.06.022>
- Reinhard, C. T., Planavsky, N. J., Robbins, L. J., Partin, C. A., Gill, B. C., Lalonde, S. V., Bekker, A., Konhauser, K. O., & Lyons, T. W. (2013). Proterozoic ocean redox and biogeochemical stasis. *Proceedings of the National Academy of Sciences*, 110, 5357–5362. <https://doi.org/10.1073/pnas.1208622110>
- Rouxel, O., Toner, B., Germain, Y., & Glazer, B. (2018). Geochemical and iron isotopic insights into hydrothermal iron oxyhydroxide deposit formation at Loihi Seamount. *Geochimica Et Cosmochimica Acta*, 220, 449–482. <https://doi.org/10.1016/j.gca.2017.09.050>
- Scott, C., Lyons, T. W., Bekker, A., Shen, Y., Poulton, S., Chu, X., & Anbar, A. (2008). Tracing the stepwise oxygenation of the Proterozoic biosphere. *Nature*, 452, 456–459.
- Scott, J. J., Glazer, B. T., & Emerson, D. (2017). Bringing microbial diversity into focus: High-resolution analysis of iron mats from the Loihi Seamount. *Environmental Microbiology*, 19, 301–316.
- Seewald, J. S., Reeves, E. P., Bach, W., Saccocia, P. J., Craddock, P. R., Shanks, W. C. III, Sylva, S. P., Pichler, T., Rosner, M., & Walsh, E. (2015). Submarine venting of magmatic volatiles in the eastern Manus Basin, Papua New Guinea. *Geochimica Et Cosmochimica Acta*, 163, 178–199. <https://doi.org/10.1016/j.gca.2015.04.023>
- Shang, M., Tang, D., Shi, X., Zhou, L., Zhou, X., Song, H., & Jiang, G. (2019). A pulse of oxygen increase in the early Mesoproterozoic ocean at ca. 1.57–1.56 Ga. *Earth and Planetary Science Letters*, 527, 115797. <https://doi.org/10.1016/j.epsl.2019.115797>
- Shapiro, R. S., & Konhauser, K. O. (2015). Hematite-coated microfossils: Primary ecological fingerprint or taphonomic oddity of the Paleoproterozoic? *Geobiology*, 13, 209–224. <https://doi.org/10.1111/gbi.12127>
- Sheen, A. I., Kendall, B., Reinhard, C. T., Creaser, R. A., Lyons, T. W., Bekker, A., Poulton, S. W., & Anbar, A. D. (2018). A model for the oceanic mass balance of rhenium and implications for the extent of Proterozoic ocean anoxia. *Geochimica Et Cosmochimica Acta*, 227, 75–95. <https://doi.org/10.1016/j.gca.2018.01.036>
- Slack, J. F. (2012). Exhalites. In W. C. Shanks III, & R. Thurston (Eds.), *Volcanogenic massive sulfide occurrence model*. (pp. 154–163). U.S. Geological Survey Scientific Investigations Report 2010–5070–C.
- Slack, J. F., Grenne, T., & Bekker, A. (2009). Seafloor-hydrothermal Si-Fe-Mn exhalites in the Pecos greenstone belt, New Mexico, and the redox state of ca. 1720 Ma deep seawater. *Geosphere*, 5, 302–314.
- Slack, J. F., Grenne, T., Bekker, A., Rouxel, O. J., & Lindberg, P. A. (2007). Suboxic deep seawater in the late Paleoproterozoic: Evidence from hematitic chert and iron formation related to seafloor-hydrothermal sulfide deposits, central Arizona, USA. *Earth and Planetary Science Letters*, 255, 243–256. <https://doi.org/10.1016/j.epsl.2006.12.018>
- Sperling, E. A., Rooney, A. D., Hays, L., Sergeev, V. N., Vorob'eva, N. G., Sergeeva, N. D., Selby, D., Johnston, D. T., & Knoll, A. H. (2014). Redox heterogeneity of subsurface waters in the Mesoproterozoic ocean. *Geobiology*, 12, 373–386. <https://doi.org/10.1111/gbi.12091>
- Spry, P. G., Peter, J. M., & Slack, J. F. (2000). Meta-exhalites as exploration guides to ore. *Reviews in Economic Geology*, 11, 163–201.
- Stampanoni, M., Groso, A., Isenegger, A., Mikuljan, G., Chen, Q., Bertrand, A., Henein, S., Betemps, R., Frommherz, U., Böhler, P., Meister, D., Lange, M., & Abela, R. (2006). Trends in synchrotron-based tomographic imaging: The SLS experience. *Proceedings of SPIE*, 6318, 63180M-1-63214.
- Sun, Z., Li, J., Huang, W., Dong, H., Little, C. T. S., & Li, J. (2015). Generation of hydrothermal Fe-Si oxyhydroxide deposit on the Southwest Indian Ridge and its implication for the origin of ancient banded iron formations. *Journal of Geophysical Research: Biogeosciences*, 120, 187–203. <https://doi.org/10.1002/2014JG002764>
- Sun, Z., Zhou, H., Glasby, G. P., Sun, Z., Yang, Q., Yin, X., & Li, J. (2013). Mineralogical characterization and formation of Fe-Si oxyhydroxide deposits from modern seafloor hydrothermal vents. *American Mineralogist*, 98, 85–97. <https://doi.org/10.2138/am.2013.4147>
- Tan, H., Verbeeck, J., Abakumov, A., & Van Tendeloo, G. (2012). Oxidation state and chemical shift investigation in transition metal oxides by EELS. *Ultramicroscopy*, 116, 24–33. <https://doi.org/10.1016/j.ultra.2012.03.002>
- Taylor, S. R., & McLennan, S. M. (1985). *The continental crust: Its composition and evolution* (p. 312). Blackwell Scientific Publications.
- Tivey, M. K. (2007). Generation of seafloor hydrothermal vent fluids and associated mineral deposits. *Oceanography*, 20, 50–65. <https://doi.org/10.5670/oceanog.2007.80>
- Toner, B. M., Berquo, T. S., Michel, F. M., Sorensen, J. V., Templeton, A. S., & Edwards, K. J. (2012). Mineralogy of iron microbial mats from Loihi Seamount. *Frontiers in Microbiological Chemistry*, 3, 1–18. <https://doi.org/10.3389/fmicb.2012.00118>
- Tostevin, R., Wood, R. A., Shields, G. A., Poulton, S. W., Guilbaud, R., Bowyer, F., Penny, A. M., He, T., Curtis, A., Hoffmann, K. H., & Clarkson, M. O. (2016). Low-oxygen waters limited habitable space for early animals. *Nature Communications*, 7(1), 1–9. <https://doi.org/10.1038/ncomms12818>
- Vander Roost, J., Daae, F. L., Steen, I. H., Thorseth, I. H., & Dahle, H. (2018). Distribution patterns of iron-oxidizing Zeta and Beta-Proteobacteria from different environmental settings at the Jan Mayen vent fields. *Frontiers in Microbiology*, 9, 3008.
- Vander Roost, J., Thorseth, I. H., & Dahle, H. (2017). Microbial analysis of Zetaproteobacteria and co-colonizers of iron mats in the Troll Wall vent field, Arctic mid-ocean Ridge. *PLoS One*, 12(9), e0185008. <https://doi.org/10.1371/journal.pone.0185008>
- Wacey, D., McLoughlin, N., Kilburn, M. R., Saunders, M., Cliff, J. B., Kong, C., Barley, M. E., & Brasier, M. D. (2013). Nanoscale analysis of pyritized microfossils reveals differential heterotrophic consumption in the ~1.9-Ga Gunflint chert. *Proceedings of the National Academy of Sciences of the United States of America*, 110, 8020–8024.

- Yang, S., Kendall, B., Lu, X., Zhang, F., & Zheng, W. (2017). Uranium isotope compositions of mid-Proterozoic black shales: Evidence for an episode of increased ocean oxygenation at 1.36 Ga and evaluation of the effect of post-depositional hydrothermal fluid flow. *Precambrian Research*, 298, 187–201. <https://doi.org/10.1016/j.precamres.2017.06.016>
- Zeng, Z., Ouyang, H., Yin, X., Chen, S., Wang, X., & Wu, L. (2012). Formation of Fe-Si-Mn oxyhydroxides at the PACMANUS hydrothermal field, eastern Manus Basin: Mineralogical and geochemical evidence. *Journal of Asian Earth Sciences*, 60, 130–146. <https://doi.org/10.1016/j.jseaes.2012.08.009>
- Zhang, K., Zhu, X., Wood, R. A., Shi, Y., Gao, Z., & Poulton, S. W. (2018). Oxygenation of the Mesoproterozoic ocean and the evolution of complex eukaryotes. *Nature Geosciences*, 11, 345–350. <https://doi.org/10.1038/s41561-018-0111-y>
- Zhang, S., Wang, X., Wang, H., Bjerrum, C. J., Hammarlund, E. U., Costa, M. M., Connelly, J. N., Zhang, B., Su, J., & Canfield, D. E. (2016). Sufficient oxygen for animal respiration 1,400 million years ago.

*Proceedings of the National Academy of Sciences*, 113, 1731–1736. <https://doi.org/10.1073/pnas.1523449113>

#### SUPPORTING INFORMATION

Additional supporting information may be found online in the Supporting Information section.

**How to cite this article:** Little CTS, Johannessen KC, Bengtson S, et al. A late Paleoproterozoic (1.74 Ga) deep-sea, low-temperature, iron-oxidizing microbial hydrothermal vent community from Arizona, USA. *Geobiology*. 2021;19:228–249. <https://doi.org/10.1111/gbi.12434>